Modeling feedback from stars and black holes in galaxy mergers

Volker Springel[1]⋆, Tiziana Di Matteo[1]† and Lars Hernquist[2]‡

[1] *Max-Planck-Institut für Astrophysik, Karl-Schwarzschild-Straße 1, 85740 Garching bei München, Germany*
[2] *Harvard-Smithsonian Center for Astrophysics, 60 Garden Street, Cambridge, MA 02138, USA*

22 October 2018

ABSTRACT
We describe techniques for incorporating feedback from star formation and black hole accretion into simulations of isolated and merging galaxies. At present, the details of these processes cannot be resolved in simulations on galactic scales. Our basic approach therefore involves forming coarse-grained representations of the properties of the interstellar medium and black hole accretion starting from basic physical assumptions, so that the impact of these effects can be included on resolved scales. We illustrate our method using a multiphase description of star-forming gas. Feedback from star formation pressurises highly overdense gas, altering its effective equation of state. We show that this allows the construction of stable galaxy models with much larger gas fractions than possible in earlier numerical work. We extend the model by including a treatment of gas accretion onto central supermassive black holes in galaxies. Assuming thermal coupling of a small fraction of the bolometric luminosity of accreting black holes to the surrounding gas, we show how this feedback regulates the growth of black holes. In gas-rich mergers of galaxies, we observe a complex interplay between starbursts and central AGN activity when the tidal interaction triggers intense nuclear inflows of gas. Once an accreting supermassive black hole has grown to a critical size, feedback terminates its further growth, and expels gas from the central region in a powerful quasar-driven wind. Our simulation methodology is therefore able to address the coupled processes of gas dynamics, star formation, and black hole accretion during the formation of galaxies.

Key words: galaxies: structure – galaxies: interactions – galaxies: active – galaxies: starburst – methods: numerical

1 INTRODUCTION

It is now recognised that galaxy collisions and mergers are relevant to a wide range of phenomena associated with both ordinary and active galaxies. The collisionless dynamics of this process is relatively well-understood. The seminal work of Toomre & Toomre (1972) using restricted N-body methods demonstrated that gravitational tidal forces between disks interacting transiently can account for the narrow tails and bridges commonly seen in morphologically peculiar galaxies. Subsequent work using self-consistent models (Barnes, 1988, 1992; Hernquist, 1992, 1993c) verified these conclusions and made it possible to extend the calculations to investigate mergers and the detailed structure of the remnants left behind. These studies showed that in many respects the remnants closely resemble elliptical galaxies, as proposed by Toomre (1977).

However, it is clear that pure stellar dynamics is not adequate to explain the extreme variety of objects linked to galaxy encounters. This possibility was already anticipated by Toomre & Toomre (1972) who suggested that collisions could "bring *deep* into a galaxy a fairly *sudden* supply of fresh fuel," leading to a period of violent, enhanced star formation. The significance of non-gravitational processes in galaxy interactions was confirmed in the 1980s when it was recognised that the brightest infrared sources seen with the IRAS satellite are invariably associated with peculiar galaxies (Sanders et al., 1988; Melnick & Mirabel, 1990). A natural interpretation of these systems is that the infrared emission is powered by a starburst, triggered through mergers.

There are also numerous studies indicating that

⋆ E-mail: volker@mpa-garching.mpg.de
† E-mail: tiziana@mpa-garching.mpg.de
‡ E-mail: lars@cfa.harvard.edu

quasars, radio galaxies, and active galactic nuclei (AGN) are preferentially found in tidally disturbed objects (for reviews, see e.g. Barnes & Hernquist, 1992; Jogee, 2004). Indeed, much circumstantial evidence suggests an evolutionary connection between merger-induced starbursts and quasar activity (Sanders et al., 1988). In addition, in recent years, strong dynamical evidence has been accumulated indicating that supermassive black holes reside at the centre of most galaxies (Kormendy & Richstone, 1995; Magorrian et al., 1998; Kormendy & Gebhardt, 2001). Moreover, a remarkable connection between supermassive black holes and the properties of their host galaxies has been discovered: the masses of central supermassive black holes are tightly correlated with the stellar velocity dispersion of their host galaxy bulges (Ferrarese & Merritt, 2000; Gebhardt et al., 2000; Tremaine et al., 2002), as well as with the mass of the spheroidal component (Magorrian et al., 1998; McLure & Dunlop, 2002; Marconi & Hunt, 2003). This strong link suggests a fundamental connection between the growth of black holes and the formation of stellar spheroids in galaxy halos (Kauffmann & Haehnelt, 2000; Volonteri et al., 2003; Wyithe & Loeb, 2003; Granato et al., 2004; Haiman et al., 2004; Di Matteo et al., 2003, 2004a, and references therein).

A better understanding of galaxy interactions and mergers will, therefore, require simultaneous accounting of the physics of interstellar gas, star formation, the growth of supermassive black holes in galactic nuclei, and various forms of feedback associated with both massive stars and AGN. As we discuss in detail below, it is not immediately obvious how these effects should be incorporated into simulations, primarily because we presently lack a sufficiently developed theory of star formation, but also because the current generation of computer models cannot resolve the complex structure of star-forming gas on the scales of whole galaxies. For these reasons, efforts to study non-gravitational processes in galaxy mergers have to rely on strong simplifications, which have often been very restrictive in previous work.

Negroponte & White (1983) used a sticky-particle treatment to show that galaxy mergers can concentrate gas in the inner regions of a remnant. Later, Hernquist (1989) and Barnes & Hernquist (1991, 1996) examined the fate of gas in minor and major mergers with a smoothed particle hydrodynamics (SPH) algorithm, neglecting star formation and feedback and approximating the structure of the interstellar medium (ISM) with an isothermal equation of state. The first serious attempts to model star formation in galaxy mergers were made by Hernquist & Mihos (1995) and Mihos & Hernquist (1996), who also used an SPH method with an isothermal gas and included a minimal form of kinetic feedback from massive stars (Mihos & Hernquist, 1994b). Gerritsen & Icke (1997) and Springel (2000) began to generalise these calculations by implementing simple approaches to allow for departures from an isothermal equation of state.

While the earlier calculations yielded many successes by providing an explicit theoretical link between galaxy mergers and starbursts, many related phenomena remain poorly understood, partly because of the approximations made in handling the consequences of feedback. In this paper, we introduce a new methodology to incorporate star formation and black hole growth into galaxy-scale simulations using a sub-resolution approach. Starting from a "microscopic"

physical theory for e.g. the ISM, we form a "macroscopic" coarse-grained representation that captures the impact of star formation and black hole growth on resolved scales. This strategy is not tied to a particular underlying model and can be used to graft any well-specified theoretical description onto the simulations. As a specific example, in what follows we will illustrate our technique using a sub-resolution multiphase model for star-forming gas developed by Springel & Hernquist (2003a). As an additional component, we will add a treatment of gas accretion onto supermassive black holes, modelled as collisionless 'sink' particles, and we treat feedback processes associated with the accretion.

Note that the use of a sub-resolution approach to include unresolved effects in simulations is a general concept also used, for example, in N-body representations of collisionless fluids, where six-dimensional phase space is discretised into fluid elements that are computationally realised as particles. Our treatment is analogous to this, except that we endow the particles with internal degrees of freedom that characterise, e.g., the thermodynamic state of star-forming gas. These internal degrees of freedom evolve in a manner consistent with the basic theory from which they are derived, enabling us to couple the "microphysics" of the ISM to the larger scale dynamics of the galaxies.

This paper is organised as follows. We first discuss the construction of compound galaxy models used in our study in Section 2. We then summarise our microscopic descriptions of star formation and black hole growth in Sections 3 and 4, respectively, and discuss aspects of our numerical treatment in Section 5. We use our models to examine the impact of various forms of feedback on isolated disks in Section 6 and major mergers in Section 7. Finally, we conclude in Section 8.

2 MODEL GALAXIES

Each galaxy in our study consists of a dark matter halo, a rotationally supported disk of gas and stars, and a central (optional) bulge. The parameters describing each component are independent, so that a wide range of morphological types can be specified. The models are constructed in a manner similar to the approach described by Hernquist (1993a) and Springel (2000), but with a number of refinements. In particular, we use halo density profiles motivated by cosmological simulations, and include pressure gradients in setting the equilibrium structure of the gas. The former consideration is important for the development of tidal features in interacting systems (Dubinski et al., 1996, 1999; Mihos et al., 1998; Springel & White, 1999), while the latter improvement is significant when the gas fraction of the disk is large, or if the gas has a relatively stiff equation of state.

2.1 Density profiles

2.1.1 Halos

In the earlier work of Hernquist (1993a), halos were described by truncated isothermal spheres with constant density cores. However, N-body simulations such as those of Dubinski & Carlberg (1991) and Navarro et al. (1996) (hereafter NFW) indicate that cosmological halos have density
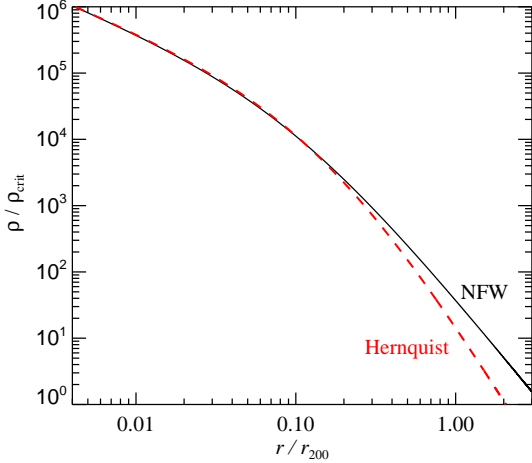
Figure 1. Density profiles of NFW and Hernquist model halos, matched to each other as described in the text. The halo has concentration $c = 10$. The *total* mass of the Hernquist model is equal to he mass of the NFW profile within the virial radius r_{200}.

profiles that are centrally peaked and drop at large radii more rapidly with radius than isothermal spheres.

In view of this, we model the dark matter mass distribution with a Hernquist (1990) profile, i.e.

$$\rho_{\rm dm}(r) = \frac{M_{\rm dm}}{2\pi} \frac{a}{r(r+a)^3}, \tag{1}$$

with cumulative mass profile $M(< r) = M_{\rm dm}\, r^2/(r + a)^2$. There are several motivations for this choice. In its inner parts, the shape of this profile agrees with the NFW fitting formula, but due to its faster decline in the outer parts, the total mass converges, allowing the construction of isolated halos without the need for an ad-hoc truncation. Furthermore, in many situations it is convenient to work with components having analytical distribution functions, as is the case for the Hernquist (1990) profile, but not for the NFW model.

To make contact with common descriptions of halos in cosmological simulations, we associate the Hernquist profile with a corresponding NFW-halo with the same dark matter mass within r_{200}, the radius at which the mean enclosed dark matter density is 200 times the critical density. We also require that the inner density profiles are equal (i.e. $\rho_{\rm dm} = \rho_{\rm NFW}$ for $r \ll r_{200}$), which implies a relation between a and the scale length r_s of the NFW profile. The latter is often given in terms of a concentration index c, conventionally defined as $c = r_{200}/r_s$, where r_s is the scale length of the NFW halo. We then have the relation

$$a = r_s \sqrt{2[\ln(1+c) - c/(1+c)]}. \tag{2}$$

For a concentration of $c = 10$, this gives $a \simeq 1.73\, r_s$. The Hernquist profile then contains 75% of its total mass within r_{200}, and 99% within $1.1\, r_{200}$.

In Figure 1, we compare the density profile of an NFW halo with a Hernquist model of the same concentration. In the inner regions, the two mass distributions match closely, while at large radii the density profiles asymptote to $\rho_{\rm NFW} \propto r^{-3}$ and $\rho_{\rm Hern} \propto r^{-4}$, respectively. At present, observations

indicate that either form can give a good description of the density profiles of actual halos when extended beyond the virial radius (Rines et al., 2000, 2002, 2003, 2004).

2.1.2 Disks and bulges

We model disk components of gas and stars with an exponential surface density profile of scale length h; i.e.

$$\Sigma_{\rm gas}(r) = \frac{M_{\rm gas}}{2\pi h^2}\, \exp(-r/h), \tag{3}$$

$$\Sigma_\star(r) = \frac{M_\star}{2\pi h^2}\, \exp(-r/h), \tag{4}$$

so that the total mass in the disk is $M_{\rm d} = (M_{\rm gas} + M_\star) = m_{\rm d} M_{\rm tot}$, where $m_{\rm d}$ is dimensionless and $M_{\rm tot}$ is the total mass of the galaxy.

The bulge is taken to be spherical, for simplicity. We also model it with a Hernquist profile:

$$\rho_{\rm b}(r) = \frac{M_{\rm b}}{2\pi} \frac{b}{r(r+b)^3}. \tag{5}$$

We treat the bulge scale length b as a free parameter that we parameterise in units of the disk scale length, and specify the bulge mass as a fraction $m_{\rm b}$ of the total mass, i.e. $M_{\rm b} = m_{\rm b} M_{\rm tot}$.

We set the disk scale length h by relating it to the angular momentum of the disk. Following Mo et al. (1998) and Springel & White (1999), we first write the total halo angular momentum of the halo as

$$J = \lambda\, G^{1/2} M_{200}^{3/2} r_{200}^{1/2} \left(\frac{2}{f_c}\right)^{1/2}, \tag{6}$$

where λ is the usual spin parameter, which we take as a free parameter of our galaxy models. The factor

$$f_c = \frac{c\left[1 - 1/(1+c)^2 - 2\ln(1+c)/(1+c)\right]}{2\left[\ln(1+c) - c/(1+c)\right]^2} \tag{7}$$

depends only on the halo concentration index. Of direct relevance for the structure of the galaxy is the fraction of the angular momentum in the disk. We typically assume $J_{\rm d} = m_{\rm d} J$, corresponding to conservation of specific angular momentum of the material that forms the disk. Assuming that the disk is centrifugally supported, this then implies a one-to-one relation between λ and h. In order to obtain this connection, we compute the disk angular momentum assuming strict centrifugal support of the disk and negligible disk thickness compared to its scale-length. Then we can write

$$J_{\rm d} = M_{\rm d} \int_0^\infty V_c(R) \left(\frac{R}{h}\right)^2 \exp\left(-\frac{R}{h}\right) {\rm d}R, \tag{8}$$

where the circular velocity is given by

$$\begin{aligned} V_c^2(R) = {} & \frac{G\left[M_{\rm dm}(< R) + M_{\rm b}(< R)\right]}{R} + \frac{2\,GM_{\rm d}}{h} y^2 \\ & \times \left[I_0(y)K_0(y) - I_1(y)K_1(y)\right]. \end{aligned} \tag{9}$$

Here $y = R/(2h)$, and the I_n and K_n are Bessel functions. Note that we will later drop the thin-disk approximation for the disk's potential in favour of an accurate representation of a thick disk. However, for the conversion of the free parameter λ into a disk scale length h, the accuracy of equation (9) is sufficient.

We specify the vertical mass distribution of the stars in the disk by giving it the profile of an isothermal sheet with radially constant scale length z_0. The 3D stellar density in the disk is hence given by

$$\rho_\star(R, z) = \frac{M_\star}{4\pi z_0 \, h^2} \, \text{sech}^2 \left(\frac{z}{2 \, z_0} \right) \exp \left(-\frac{R}{h} \right). \tag{10}$$

We treat z_0 as a free parameter that effectively determines the 'temperature' of the disk, and set the velocity distribution of the stars such that this scale-height is self-consistently maintained in the full 3D potential of the galaxy model.

However, a similar freedom is not available for the gas, because once cooling and star formation processes are taken into account, we cannot choose the temperature freely. Rather, in a broad class of models the gas will stay close to an (effective) equation of state of the form $P = P(\rho)$, implying a tight relation of gas pressure and gas density. Examples for such situations include isothermal gas, or the subresolution multiphase model by Springel & Hernquist (2003a). For a given surface density, the vertical structure of the gas disk then arises as a result of self-gravity and the pressure given by this equation of state, leaving no freedom for prescribing a certain vertical profile. In this situation, the vertical structure has to be computed self-consistently, as discussed next.

2.1.3   *Vertical structure of the gas disk*

We assume that the vertical structure of the gas disk in our axisymmetric galaxy models is governed by hydrostatic equilibrium, i.e.

$$-\frac{1}{\rho_g} \frac{\partial P}{\partial z} - \frac{\partial \Phi}{\partial z} = 0, \tag{11}$$

where Φ is the total gravitational potential of all mass components. This equation can be rewritten as

$$\frac{\partial \rho_g}{\partial z} = -\frac{\rho_g^2}{\gamma P} \frac{\partial \Phi}{\partial z}, \tag{12}$$

where $\gamma = \frac{d \ln P}{d \ln \rho}$ is the local polytropic index of the equation of state. Note that for a given potential Φ, the solution of this equation is determined by the integral constraint

$$\Sigma_{\text{gas}}(R, z) = \int \rho_g(R, z) \, dz, \tag{13}$$

where $\Sigma_{\text{gas}}(r)$ is the surface mass density we prescribed in equation (3). Assuming a given potential for the moment, we solve equations (12) and (13) by integrating the differential equation for a chosen central density value in the $z = 0$ midplane. This chosen starting value is then adjusted until we recover the desired surface density for the integrated vertical structure of the gas layer. We carry out this process as a function of radius, using a fine logarithmic grid of points in the $R-z$ plane to represent the axisymmetric gas density distribution.

2.2   Evaluating the potential

The above invokes the problem of determining the potential and the resulting gas distribution *self-consistently*. We address this problem by an iterative method. Starting with
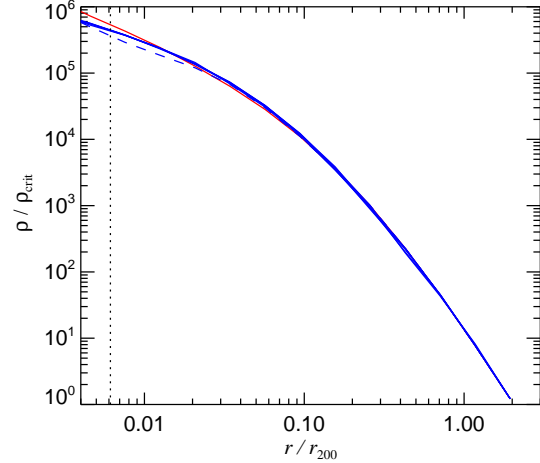

Figure 2. Time evolution of a Hernquist dark matter halo with initial conditions constructed in the way described in this paper. The initially realised input profile is the thin red line. Because the approximation of a locally Gaussian velocity distribution is not exact, the central profile is not in perfect equilibrium in the beginning. As a result, the density in the centre fluctuates downwards on a short timescale of order the crossing time, and then relaxes to a slightly softer central profile. After time $t = 0.08$ (in units of the dynamical time, $t_{\text{dyn}} = r_{200}/v_{200}$, of the halo), the deviation is close to its maximum (dashed line). Already at $t = 0.16$, however, a stable profile is reached, which then remains essentially invariant with time, as illustrated by the further output times that are overplotted (at times $t = 0.24, 0.32, 0.48,$ and 0.64). The vertical dotted line marks the scale below which the force law is softened compared to the Newtonian value.

a guess for an initial potential, we compute the implied vertical gas structure as described above, treating the potential as fixed. Then, we recompute the potential for the updated gas distribution, and repeat the whole process. In doing this, the potential and the gas distribution converge quickly, within a few iterations, to a self-consistent solution.

However, in doing this, we also need a method to accurately compute the potential and the resulting force field for the radially varying density stratification of the gas. Since we want to be able to set up quite massive gas disks that are in equilibrium right from the start, we cannot utilise simple thin-disk approximations, but rather need to compute the full potential accurately. The generality of the gas distributions used here makes this a non-trivial exercise.

We use a somewhat contrived, yet extremely flexible solution for this task. We set up a discretised mass distribution that represents the desired disk components accurately, and then compute the potential numerically with a hierarchical multipole expansion based on a tree code. For a given (current) mass model of the galaxy, we use for this purpose a suitably distorted grid of particles of typically $2048 \times 64 \times 64$ particles per component (the different numbers refer to radial, azimuthal, and vertical directions, respectively). While we find that this gives sufficient accuracy for our purposes, we note that the number of particles can be easily made much larger to generate a still smoother potential, if needed. Unlike in a normal N-body code, we are here not interested
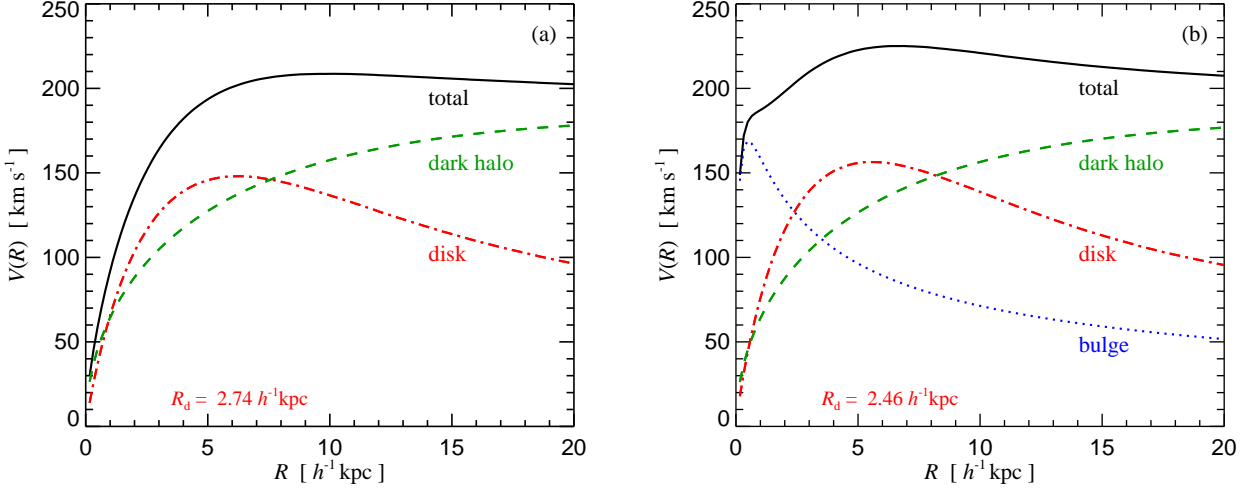
Figure 3. Rotation curves of model galaxies with the following parameters: (a) $v_{200} = 160$ km s^{-1}, $c = 9$, $m_{\rm d} = 0.041$, $m_{\rm b} = 0$, $f_{\rm gas} = 0.1$, $\lambda = 0.033$, $J_{\rm d} = 0.041$, $z_0 = 0.2$; (b) same as model (a) but with $m_{\rm b} = 0.01367$. The resulting disk scale lengths are $2.74\,h^{-1}$kpc and $2.46\,h^{-1}$kpc, respectively.

in evaluating the forces or the values of the potential for all these particles. We only use them as markers for the mass, and instead compute the potential at a fixed set of spatial coordinates. The work required for this potential computation then scales only with $\log(N)$. The primary cost of making N large lies therefore in the memory consumed on the computer, and not in the CPU time. The potential and force field of the spherical mass distributions used for the dark matter halo and the bulge are known analytically, so we simply add them to the result obtained with the tree for the disk components.

2.3 Velocity structure

Once the full density distribution has been determined, we compute approximations for the velocity structure of the collisionless and gaseous components. For the dark matter and stars in the bulge, we assume that the velocity distribution function only depends on energy E and the L_z-component of the angular momentum. Then, mixed second order moments of the velocity distribution vanish, $\langle v_R v_z \rangle = \langle v_z v_\phi \rangle = \langle v_R v_\phi \rangle = 0$, as well as the first moments in radial and vertical directions, $\langle v_R \rangle = \langle v_z \rangle = 0$. The velocity distribution can then be approximated as a triaxial Gaussian with axes aligned with the axisymmetric coordinate system. The non-vanishing second-moments can be obtained with the Jeans equations. We have

$$\langle v_z^2 \rangle = \langle v_R^2 \rangle = \frac{1}{\rho} \int_z^\infty \rho(z', R) \frac{\partial \Phi}{\partial z'}\, dz', \qquad (14)$$

where ρ is the density of the mass component under consideration. For the azimuthal direction we have

$$\langle v_\phi^2 \rangle = \langle v_R^2 \rangle + \frac{R}{\rho} \frac{\partial \left(\rho \langle v_R^2 \rangle \right)}{\partial R} + v_c^2, \qquad (15)$$

where

$$v_c^2 = R \frac{\partial \Phi}{\partial R} \qquad (16)$$

is the circular velocity.

In the azimuthal direction, there can be a mean streaming component $\langle v_\phi \rangle$, which is not determined by the Jeans equations. Once it is specified, the dispersion of the Gaussian velocity distribution in the azimuthal direction is given by

$$\sigma_\phi^2 = \langle v_\phi^2 \rangle - \langle v_\phi \rangle^2. \qquad (17)$$

For the stellar bulge, we set $\langle v_\phi \rangle$ to zero, meaning that the bulge is assumed to have no net rotation. For the dark matter halo, we assume that it has the same specific angular momentum as the disk material. For simplicity, we impart this angular momentum by making $\langle v_\phi \rangle$ a fixed fraction of the circular velocity, i.e. $\langle v_\phi \rangle = f_s v_c$ (Springel & White, 1999). Note that we then have $f_s \ll 1$, i.e. the net streaming of the resulting dark halo is quite small.

The velocity structure of the stellar disk can in principle be much more complicated, and it will in general have a distribution function that does not only depend on E and L_z. For simplicity, we however continue to approximate the velocity distribution with a triaxial Gaussian that is aligned with the axisymmetric coordinated vectors.

As Hernquist (1993a) points out, observationally there is good evidence that $\langle v_R^2 \rangle$ is proportional to $\langle v_z^2 \rangle$ for the stellar disk. We hence assume $\sigma_R^2 = \langle v_R^2 \rangle = f_R \langle v_z^2 \rangle$. Note that larger values of f_R will increase the Toomre Q parameter, making the disk more stable against axisymmetric perturbations. In most of our default models, we actually set $f_R = 1$ which corresponds to the approximations made for the dark halo and the bulge. Note that the Toomre Q also varies in response to the vertical dispersion $\langle v_z^2 \rangle$ which sensitively depends on the assumed disk thickness.

To specify the mean streaming, we employ the epicyclic approximation, which relates the radial and vertical dispersions in the stellar disk:

$$\sigma_\phi^2 = \frac{\sigma_R^2}{\eta^2}, \qquad (18)$$

where

$$\eta^2 = \frac{4}{R} \frac{\partial \Phi}{\partial R} \left(\frac{3}{R} \frac{\partial \Phi}{\partial R} + \frac{\partial^2 \Phi}{\partial R^2} \right)^{-1}. \tag{19}$$

Using equation (15) for $\langle v_\phi^2 \rangle$, we then set the streaming velocity for the stellar disk as

$$\langle v_\phi \rangle = \left(\langle v_\phi^2 \rangle - \frac{\sigma_R^2}{\eta^2} \right)^{1/2}. \tag{20}$$

This completes the specification of the velocity structure of the collisionless components.

For the gas, we deal with a single valued velocity field, where only the azimuthal streaming velocity has to be specified. The latter is determined by the radial balance between gravity on one hand, and centrifugal and pressure support on the other hand. Specifically, we here have

$$v_{\phi,\text{gas}}^2 = R \left(\frac{\partial \Phi}{\partial R} + \frac{1}{\rho_g} \frac{\partial P}{\partial R} \right). \tag{21}$$

Note that the gas temperature at each coordinate is given by the equation of state based on the self-consistent mass distribution derived above.

We carry out the integrations over the force field needed in the Jeans equations with the help of a fine logarithmic grid in the R-z-plane. This grid is also used to tabulate the final velocity dispersion fields. The differentiations needed in equation (15), for example, are approximated by finite-differencing off this grid. Once all of the density and velocity distributions have been computed, we initialise particle coordinates and velocities by drawing randomly from the respective distributions. Values for the velocity structure at individual particle coordinates are obtained by bilinear interpolation of the R-z grid.

Kazantzidis et al. (2004) recently examined the accuracy of initialising spherically symmetric dark matter halos with a Gaussian velocity distribution with dispersion derived from the Jeans equations. They found that the innermost parts of halos are not precisely in equilibrium when this approximation is applied. As a result, the core relaxes within the first few crossing times to a density profile which lies slightly below the input profile in the centre, such that the central cusp becomes softer. Using a more accurate computation of the velocity distribution function that takes higher order moments into account, they also demonstrated that this behaviour can in principle be avoided.

In Fig. 2, we show an example of this effect. To illustrate this in a manner unaffected by two-body relaxation we have set-up a pure dark matter halo with 4 million particles using our code for constructing compound galaxies. When evolved forward in time, the density profile in the very centre fluctuates below the desired input value during the first crossing times. Afterwards, the density profile shows no further secular evolution and stays extremely stable for times of order the Hubble time. The magnitude of the initial relaxation effect appears to be consistent with what Kazantzidis et al. (2004) found. However, we argue that this perturbation is acceptably small for our purposes. This is because the effect on the central dark matter profile is really quite moderate, and occurs in a radial region that is already dominated by baryonic physics when a disk component is included as well. In fact, our disk galaxy models show remarkable little

secular relaxation when started from initial conditions constructed in the above fashion, even for high gas fractions. We here benefit from the included treatment of gas pressure forces and the improved potential computation compared to previous methods (Hernquist, 1993a; Springel, 2000).

2.4 Galaxy model parameters

In summary, we specify a disk galaxy model with the following parameters:

• The total mass is given in terms of a 'virial velocity', v_{200}. We set $M_{\text{tot}} = v_{200}^3/(10GH_0)$.
• The total mass of the disk is given in terms of a dimensionless fraction m_d of this mass, i.e. $M_{\text{disk}} = m_d M_{\text{tot}}$. Likewise, the mass of the bulge is given in terms of a dimensionless fraction m_b of the total, i.e. $M_{\text{bulge}} = m_b M_{\text{tot}}$. The rest of the total mass is in the dark matter halo.
• A fraction f_{gas} of the disk is assumed to be in gaseous form, the rest in stellar form. The bulge is taken to be completely stellar.
• The stellar disk is assumed to have an exponential profile with radially constant vertical scale-height z_0. We specify the latter in units of the radial disk scale length, and typically use $z_0 \simeq 0.1 - 0.2\, h$.
• Similarly, the bulge scale length is specified as a fraction of the radial disk scale length.
• A value for the spin parameter λ of the halo is selected. Its value effectively determines the radial scale length of the disk.

In Figure 3, we show rotation curves for two galaxy models that we use in many of the numerical simulations in this study. The two models have a mass comparable to the Milky Way, $M_{\text{tot}} = 0.98 \times 10^{12}\, h^{-1} \text{M}_\odot$, corresponding to a virial velocity $v_{200} = 160\, \text{km s}^{-1}$. Their disk mass is specified by $m_d = 0.041$. The model that includes a bulge (shown on the right) has a rotation curve very similar to the one used by Hernquist (1993a). Note that the model on the left, with its slowly rising rotation curve due to the absence of a bulge (a similar model was used, e.g., by Mihos & Hernquist, 1994b), is more susceptible to tidal perturbations.

3 STAR FORMATION AND STELLAR FEEDBACK

Current state of the art simulations lack the dynamic range needed to follow the detailed structure of star-forming gas on scales characterising entire galaxies. For example, in simulations like those presented in the following sections of this paper, tens or hundreds of thousands of particles are used to characterise the gas in individual disk galaxies, so that each particle represents roughly $\gtrsim 10^5\, \text{M}_\odot$ of interstellar material for typical disk gas fractions. However, in order to resolve bound structures in SPH, an object must contain at least a number of particles comparable to the number averaged over when forming smoothed quantities. Here, we set this parameter typically to be $\simeq 64$ neighbouring particles, so that the simulations cannot resolve bound objects with masses smaller than about $\sim 6 \times 10^6 \text{M}_\odot$. Simulations with total particle numbers 100 times larger than those presented here are feasible, but even then we would not able to resolve
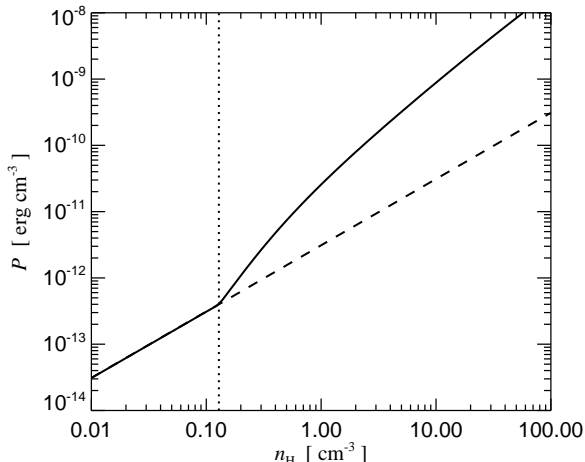
Figure 4. Effective equation of state for the star-forming gas (solid curve). We show the effective pressure measured in cgs units as a function of the gas density in hydrogen atoms per cubic centimetre. The vertical dotted line delineates the transition from an isothermal gas (dashed) at temperature 10^4 K to the regime governed by an effective pressure in our multiphase model. For the particular parameters chosen in this example, the transition density lies at $0.128\,\text{cm}^{-3}$.

self-gravitating structures with masses $\lesssim 10^5\,\text{M}_\odot$. Furthermore, such calculations would be limited to a spatial resolution of order ~ 20 pc. These mass and spatial scales are barely sufficient to resolve individual giant molecular clouds and are inadequate to describe the details of the star-forming gas contained within them.

More seriously, there is at present no complete theory for star formation, so the important physics is not well understood. Even if the simulations could include the entire dynamic range needed to resolve the essentials of star formation on galactic scales, the description of this process would therefore still have to be parameterised using bulk averaged quantities. For these reasons, we are motivated to adopt an approach in which we discard detailed information about star-forming gas in favour of a procedure that captures generic consequences of star formation and associated feedback effects on resolved scales. In this manner, we do not attempt to characterise all aspects of the physics but instead seek to identify general trends.

As an illustration of our procedure, we employ the sub-resolution multiphase model for star-forming gas developed by Springel & Hernquist (2003a, hereafter SH03). In this picture, the ISM is pictured to consist of cold clouds where stars form, embedded in a hot, pressure-confining phase. The gas is assumed to be thermally unstable to the onset of a two-phase medium at densities above a threshold ρ_{th}. The fraction of mass in the two phases at higher densities is set by star formation and feedback, evaporation of the cold clouds through thermal conduction, and the growth of clouds owing to radiative cooling. The rates at which the mass in the two phases evolve are given by eqns. (5) and (6) in SH03. The thermal budget of the cold clouds and hot gas is determined by the same effects and evolves according to eqns. (8) and (9) in SH03.

Our coarse-grained representation of this model reduces largely to two principle ingredients: (1) a star formation prescription or "law", and (2) an effective equation of state (EOS) for the ISM. For the former, we adopt a rate motivated by observations (Kennicutt, 1989, 1998):

$$\frac{\text{d}\rho_*}{\text{d}t} = (1 - \beta)\frac{\rho_c}{t_*}, \tag{22}$$

where $\text{d}\rho_*/\text{d}t$ is the star formation rate, β depends on the initial mass function (IMF) and is the mass fraction of stars that die immediately as supernovae, ρ_c is the density of cold clouds, and t_* is a characteristic timescale. For a Salpeter type IMF we have $\beta \approx 0.1$. In our multiphase picture, $\rho_c \approx \rho$, where ρ is the total gas density (see Fig. 1 in SH03). A good match to observations is obtained if t_* is assumed to be proportional to the local dynamical time

$$t_*(\rho) = t_*^0 \left(\frac{\rho}{\rho_{\text{th}}}\right)^{-1/2}, \tag{23}$$

where t_*^0 is a constant parameter.

The effective equation of state (EOS) of the gas in this model is given by

$$P_{\text{eff}} = (\gamma - 1)\,(\rho_h u_h + \rho_c u_c), \tag{24}$$

where ρ_h and u_h are the density and specific thermal energy of the hot phase, with similar quantities defined for the cold clouds, while $\gamma = 5/3$ is the adiabatic index of the gas. In detail, the EOS depends on the values of the parameters in our model.

As described by SH03, the parameter values are constrained by the nature of the cooling curve for the gas and by requiring that the EOS be a continuous function of density. SH03 also showed that if star formation is rapid compared with adiabatic heating or cooling owing to the motion of the gas, then the multiphase picture leads to a cycle of self-regulated star formation where, in equilibrium, the growth of cold clouds is balanced by their evaporation from supernova feedback. Under these conditions and for a given IMF, the EOS is determined by three parameters: the constant appearing in the star formation law, t_*^0, a normalisation of the cloud evaporation rate, A_0, and a supernova "temperature", T_{SN}, that reflects the heating rate from a population of supernova for the adopted IMF. The requirement that the gas be thermally unstable at densities above ρ_{th} fixes the ratio $T_{\text{SN}}/A_0 \approx 10^5$ while in the self-regulated regime, the condition that the EOS be continuous implies that ρ_{th} depends mainly on the ratios T_{SN}/A_0 and T_{SN}/t_*^0 (see eqn. 23 of SH03).

In Figure 4, we show an example of the form of our effective EOS for the parameter choices $T_{\text{SN}} = 10^8$, $A_0 = 1000$, and $t_*^0 = 2.1$ Gyrs. For an isolated disk galaxy, these values reproduce the observed correlation between star formation and gas density (see Figs. 2-3 of SH03). For densities higher than ρ_{th}, the EOS shown in Figure 4 is fitted to an accuracy of 1% by (Robertson et al., 2004)

$$\log P_{\text{eff}} = 0.050\,(\log n_{\text{H}})^3 - 0.246\,(\log n_{\text{H}})^2 + \tag{25}$$
$$+ 1.749 \log n_{\text{H}} - 10.6\,.$$

The important features of our EOS can be seen from Figure 4. If the gas were isothermal at all densities, the effective pressure, P_{eff}, would increase linearly with density,

as indicated by the dashed line for densities higher than ρ_{th}. However, when we account for supernova feedback in our multiphase model, the EOS in star-forming gas is stiffer (solid curve in Figure 4). Suppose a region at densities lower than ρ_{th} is compressed. If the gas were isothermal, the effective pressure would increase proportional to the density. However, in our multiphase model, once $\rho > \rho_{\text{th}}$, the gas is thermally unstable and stars can form. As the density rises further, the star formation rate increases even faster, as does the rate of energy injection into the gas from supernova. If this feedback energy is retained by the gas, its effective EOS of state will be stiffer than isothermal.

The concept of an "effective equation of state" thus incorporates the impact of local feedback in regulating the thermodynamic properties of the ISM. Using this concept, we can describe the dynamics of star-forming gas on galactic scales and account for the consequences of stellar feedback on large scales. For example, the dynamical stability of a pure gas disk to axisymmetric perturbations is determined by the condition (Toomre, 1964)

$$Q \equiv \frac{c_s \kappa}{\pi G \Sigma} > 1, \tag{26}$$

where c_s is the sound speed, κ is the epicyclic frequency, and Σ is the gas surface density. This relation represents a competition between the stabilising influences of pressure (c_s) and angular momentum (κ) against the destabilising effect of gravity (Σ). If we consider a small region in the disk, the appropriate EOS with which to compute c_s is not one that captures the detailed structure of the ISM, but an effective EOS on the scale of the instability. For parameters typical of galactic disks, the fastest growing mode has a wavelength that is comparable to the size of the disk (Binney & Tremaine, 1987), and so stability is determined by the response of the ISM to compressions on this scale.

In the absence of a complete theory for the ISM, the choices for the star formation law and effective equation of state are not unique. For example, Barnes (2004) has recently proposed a star formation prescription that is based on the rate at which gas generates entropy in shocks. His numerical tests indicate that this formalism may yield a better match to observations of interacting galaxies than a purely density-dependent star formation law.

In our approach, we will consider the macroscopic star formation law and effective equation of state as elements of our description that can in principle be varied independently to isolate the large-scale physics that regulates star formation in colliding and merging galaxies. In particular, we will also consider simulations where we "soften" the EOS by linearly interpolating between that for the standard implementation of our multiphase model and an isothermal EOS. We will denote this softening by a parameter q_{EOS} so that $q_{\text{EOS}} = 1$ will correspond to e.g. the "stiff" EOS shown by the solid curve in Figure 4, and $q_{\text{EOS}} = 0$ will correspond to the "soft," isothermal EOS, indicated by the dashed curve in Figure 4.

While we do not expect that the effective EOS employed here is a precise description of real star-forming gas, the approach that we adopt is flexible and can be applied to any well-specified theory for the ISM. In particular, Springel & Hernquist (2003b) have shown that our coarse-graining procedure leads to a numerically converged estimate for the

cosmic star formation history of the Universe (Hernquist & Springel, 2003) that agrees well with low redshift observations.

The hybrid multiphase model of SH03 also includes a phenomenological representation of galactic winds. In this picture, some of the energy available from supernova feedback is tapped to drive an outflow if the star formation rate exceeds a critical threshold. For simplicity, we do not include this additional mode of feedback in the present study.

4   BLACK HOLE ACCRETION AND AGN FEEDBACK

It is now widely believed that black hole growth and associated feedback energy from this process may be important for a variety of phenomena related to the evolution of ordinary galaxies as well as unusual behaviour in quasars, starbursts, and AGN. It has been suggested that the $M_{\text{BH}} - \sigma$ relation may arise if strong outflows are produced in response to a major phase of black hole accretion, which via their interaction with the surrounding gas would inhibit any further accretion and hence black hole growth (Silk & Rees, 1998; Fabian, 1999; King, 2003; Wyithe & Loeb, 2003). Indeed, X-ray observations of a number of quasars (mostly broad absorption line systems) reveal significant absorption, implying large outflows with a kinetic power corresponding to a significant fraction of the AGN bolometric luminosity (Chartas et al., 2003; Crenshaw et al., 2003; Pounds et al., 2003). In the case of radio-loud QSO, there is also evidence that up to half of the total power is injected in the form of jets (Rawlings & Saunders, 1991; Tavecchio et al., 2000). Inevitably, such outflows must have a strong impact on the host galaxies. Models of interacting and merging galaxies should, therefore, account for feedback from both star formation and accretion onto central, supermassive black holes. Note that black hole (BH) accretion is expected to be responsible for the majority of the BH mass growth and to provide sufficient energy supply for driving associated outflows.

As with star formation, current numerical simulations cannot resolve the properties of the accretion flow around nuclear black holes on galactic scales. For example, consider a black hole of mass M_{BH} accreting spherically from a stationary, uniform distribution of gas whose sound speed at infinity is c_∞. The gravitational radius of influence of the black hole is then (Bondi, 1952)

$$r_{\text{B}} = \frac{G M_{\text{BH}}}{c_\infty^2}. \tag{27}$$

For a black hole of mass $M_{\text{BH}} = 10^7\,M_\odot$ in a gas with a sound speed $c_\infty = 30\,\text{km/sec}$, this is numerically

$$r_{\text{B}} = 50\,\text{pc}\left(\frac{M_{\text{BH}}}{10^7\,M_\odot}\right)\left(\frac{c_\infty}{30\,\text{km/sec}}\right)^{-2}. \tag{28}$$

The Schwarzschild radius of a black hole of this mass is

$$r_{\text{s}} \equiv \frac{2 G M_{\text{BH}}}{c^2} = 10^{-6}\,\text{pc}\left(\frac{M_{\text{BH}}}{10^7\,M_\odot}\right). \tag{29}$$

Our understanding of the nature of accretion onto supermassive black holes is sufficiently poor that it is not clear what range in spatial scales would be required to obtain an

accurate description of the impact of black hole growth and feedback on galactic scales. However, given the relatively poor resolution that can be achieved in simulations like those presented here, it is clear that they cannot represent the full complexities of this process in any detail. By analogy with out treatment of star formation and supernova feedback, we are hence led to adopt a coarse-graining procedure.

In what follows, we use an effective sub-resolution model to characterise the growth of supermassive black holes in galactic nuclei and the consequences of feedback from accretion on surrounding gas. Technically, we represent black holes by collisionless particles that can grow in mass by accreting gas from their environments. A fraction of the radiative energy released by the accreted material will be assumed to couple thermally to nearby gas and influence its motion and thermodynamic state.

Like our procedure for coarse-graining the ISM, our method is flexible and can be applied to any model for black hole accretion. As a starting point, we relate the (unresolved) accretion onto the black hole to the large scale (resolved) gas distribution using a Bondi-Hoyle-Lyttleton parameterisation (Bondi, 1952; Bondi & Hoyle, 1944; Hoyle & Lyttleton, 1939). In this description, the accretion rate onto the black hole is given by

$$\dot{M}_{\mathrm{B}} = \frac{4\pi\,\alpha\,G^2 M_{\mathrm{BH}}^2\,\rho}{(c_s^2 + v^2)^{3/2}}\,, \tag{30}$$

where ρ and c_s are the density and sound speed of the gas, respectively, α is a dimensionless parameter, and v is the velocity of the black hole relative to the gas. We will also assume that the accretion is limited to the Eddington rate

$$\dot{M}_{\mathrm{Edd}} \equiv \frac{4\pi\,G\,M_{\mathrm{BH}}\,m_{\mathrm{p}}}{\epsilon_{\mathrm{r}}\,\sigma_{\mathrm{T}}\,c}\,, \tag{31}$$

where m_{p} is the proton mass, σ_{T} is the Thomson cross-section, and ϵ_{r} is the radiative efficiency. The latter is related to the radiated luminosity, L_{r} and accretion rate, $\dot{M}_{\mathrm{BH}}$, by

$$\epsilon_{\mathrm{r}} = \frac{L_{\mathrm{r}}}{\dot{M}_{\mathrm{BH}}\,c^2}\,, \tag{32}$$

i.e. it simply gives the mass to energy conversion efficiency set by the amount of energy that can be extracted from the innermost stable orbit of an accretion disk around a black hole. For the rest of this study, we adopt a fixed value of $\epsilon_{\mathrm{r}} = 0.1$, which is the mean value for radiatively efficient Shakura & Sunyaev (1973) accretion onto a Schwarzschild black hole. We ignore the possibility of radiatively inefficient accretion phases. The accretion rate is then

$$\dot{M}_{\mathrm{BH}} = \min(\dot{M}_{\mathrm{Edd}}\,, \dot{M}_{\mathrm{B}})\,. \tag{33}$$

We will assume that some fraction ϵ_{f} of the radiated luminosity L_{r} can couple thermally (and isotropically) to surrounding gas in the form of feedback energy, viz.

$$\dot{E}_{\mathrm{feed}} = \epsilon_{\mathrm{f}}\,L_{\mathrm{r}} = \epsilon_{\mathrm{f}}\,\epsilon_{\mathrm{r}}\,\dot{M}_{\mathrm{BH}}\,c^2\,. \tag{34}$$

Characteristically we take $\epsilon_{\mathrm{f}} \sim 0.05$, so that $\sim 0.5\%$ of the accreted rest mass energy is available as feedback. This value fixes the normalisation of the $M_{\mathrm{BH}} - \sigma$ relation, and brings it into agreement with current observations (Di Matteo et al., 2004b).
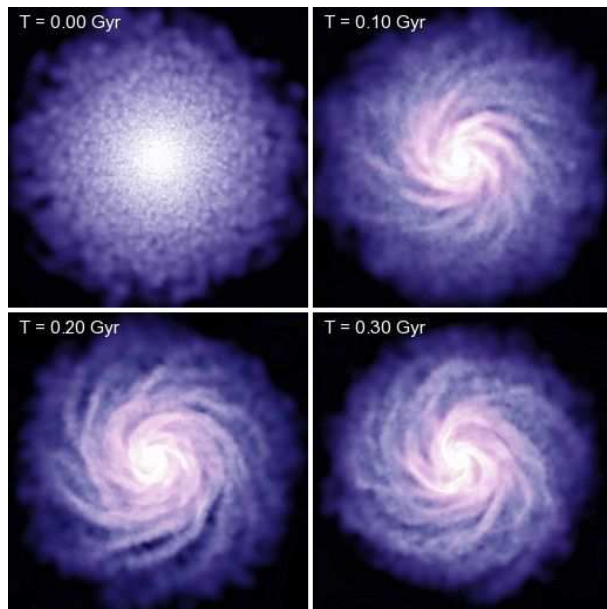
Figure 5. Evolution of the gaseous disk in an isolated galaxy model with a bulge component. A fraction $f_{\mathrm{gas}} = 0.1$ of the disk mass is in gas. The remaining 90% is in old stars. The panels show a face-on projection of the gas in the disk, and measure $30\,h^{-1}\mathrm{kpc}$ on a side. The colour-coding indicates both gas density (in terms of intensity) and local gas temperature (in terms of colour hue). Time in Gyrs is indicated in the upper left corner of each frame.

5 NUMERICAL APPROACH

Nothing in our formulation of supernova and black hole feedback is tied to a particular numerical scheme for solving the dynamical equations for the gas and collisionless matter. Our sub-resolution models and coarse-graining procedure could be incorporated into either particle- or grid-based methods. In our simulations, we employ an N-body algorithm for the collisionless material which, in our case, includes dark matter, stars, and black holes. For the hydrodynamics, we employ a smoothed particle hydrodynamics (SPH) code which represents fluids elements by particles (Lucy, 1977; Gingold & Monaghan, 1977; Monaghan, 1992). In SPH, fluid properties at a given point are estimated by local kernel-averaging over neighbouring particles, and smoothed versions of the equations of hydrodynamics are solved for the evolution of the fluid.

The particular code we use is an improved and updated version of GADGET (Springel et al., 2001). The code implements a TreeSPH algorithm (Hernquist & Katz, 1989) where gravitational forces are computed with a hierarchical tree method (Barnes & Hut, 1986) and SPH is used for the hydrodynamics. In the new version GADGET2 employed here, the hydrodynamical equations are solved using a fully conservative technique (Springel & Hernquist, 2002), which maintains strict entropy and energy conservation even when smoothing lengths vary adaptively (Hernquist, 1993b).

Besides gravity and hydrodynamics, the code follows radiative cooling processes of an optically thin primordial plasma of helium and hydrogen in the presence of an UV background (Katz et al., 1996). Star formation and the dynamics of the highly overdense gas are treated with the mul-

tiphase model described earlier. Independent star particles are stochastically spawned out of the gas phase (Springel & Hernquist, 2003a), thereby avoiding artificial coupling between gaseous and collisionless matter.

Black holes are represented by collisionless "sink" particles which only feel gravitational forces. For these particles, we compute estimates for the gas density in their local environments, in the same fashion as it is done for normal SPH particles. Similarly, we also determine the average gas temperature in the local SPH smoothing environment around black hole particles, as well as the gas bulk velocity relative to the black holes. These quantities are then used to estimate the black hole accretion rates, based on the equations specified in the previous section.

To implement the actual accretion, we follow a similar stochastic approach as it is applied for regular star formation. To this end, we compute for each gas particle j around a black hole a probability

$$p_j = \frac{w_j \dot{M}_{\mathrm{BH}} \Delta t}{\rho} \tag{35}$$

for being absorbed by the BH. Here $\dot{M}_{\mathrm{BH}}$ is the BH accretion rate, Δt is the timestep, ρ is the gas density estimated at the position of the black hole, and w_j is the kernel weight of the gas particle relative to the BH. We then draw random numbers x_j uniformly distributed in the interval $[0, 1[$ and compare them with the p_j. For $x_j < p_j$, the gas particle is absorbed by the black hole, including its momentum. On average, this procedure ensures that the BH particle accretes the right amount of gas consistent with the estimated accretion rate $\dot{M}_{\mathrm{BH}}$.

However, because the accretion rate depends sensitively on M_{BH}, this procedure would be quite noisy under conditions of poor resolution, where accreting a single gas particle can change the BH particle mass by a substantial factor. We circumvent this problem by giving the sink particle an internal degree of freedom that describes the BH mass in a smooth fashion. The value of this variable represents the BH mass for the case of ideal resolution where the gas mass is not discretised. The real dynamical mass of the sink particle tracks this internal mass closely, albeit with stochastic fluctuations around it. For this reason, we use the internal mass for computing the accretion rates, while the growth of the hole is followed both in terms of the internal mass and the actual dynamical mass. The latter increases in discrete steps when whole gas particles are absorbed, but follows the internal variable in the mean, with fluctuations that become progressively smaller for better resolution. Using this procedure we can reliably follow the growth of black holes in terms of their internal mass variable even in halos with just a few hundred particles, which is particularly important for cosmological simulations, where the earliest generations of galaxies are typically not very well resolved. Note that we conserve momentum when gas particles are absorbed by BH sink particles. If the BH is moving relative to the gas and has a high accretion rate, this can effectively act like a friction force which reduces the relative motion.

Together with the accretion, we compute the rate of feedback associated with the black hole growth. This energy is added kernel-weighted to the thermal reservoir of the gas in the local environment around the black hole. Note that if the local cooling rate of the gas is not high enough to radiate

away all of this energy on a short timescale, an increase of the gas sound speed occurs which can then throttle the accretion in the Bondi-dominated regime.

In the final stages of a galaxy merger, the cores of the galaxies coalesce to form a single dark matter halo, and a single stellar system. Presumably, this also means that a central binary system of two supermassive black holes is formed, which may subsequently harden and eventually lead to physical collision and merger of the black holes themselves. However, it is a controversial question how long it would take to harden the black hole binary by stellar-dynamical (Makino & Funato, 2004) or hydrodynamical processes (Escala et al., 2004) until finally gravitational wave emission becomes important, leading to quick orbital decay. If black hole merger processes were inefficient, it should be a common situation that a third supermassive black hole is brought in by the next galaxy merger. This black hole could then interact with the binary and lead to sling-shot ejection of one of the holes, with the remaining pair being ejected in the opposite direction. As this may seriously impair the growth of black holes to the large masses that are observed, the existence of supermassive black holes may be taken as circumstantial evidence that BH binaries probably do merge. We therefore assume that two black hole particles merge instantly if they come within each others's smoothing lengths, and their relative velocities are at the same time smaller than the local sound speed. Note that as with the accretion itself, we lack the dynamic range in simulations of whole galaxies to study the hardening process of black hole binaries directly.

6   ISOLATED DISK GALAXIES

We have run a series of simulations of isolated galaxies using the methods described in Section 2 to initialise them. In the following, we examine their stability using models with and without bulges, having the rotation curves shown in Figure 3. The structure of these models was motivated by properties of galaxies like the Milky Way and to enable us to compare our results with earlier work, such as Hernquist & Mihos (1995) and Mihos & Hernquist (1996). Here, we focus on the effect of varying the stiffness of the EOS and the gas fraction in the disk. A significant advantage of our formalism is that we are now able to construct stable equilibrium models with a larger gas fraction than possible in previous studies.

6.1   Stability of models without black holes

In order to facilitate comparison between different cases, in this section we fix the parameters associated with our multiphase model and vary only the disk gas fraction and the stiffness of the effective EOS. For definiteness, we take $t_*^0 = 8.4\,\mathrm{Gyrs}$, $A_0 = 4000$, and $T_{\mathrm{SN}} = 4 \times 10^8$. This choice for t_*^0 is a factor of four larger than that employed by SH03 to match the Kennicutt Law. However, we find that for our isolated galaxies, $t_*^0 = 2.1\,\mathrm{Gyrs}$ yields global star formation rates $\gtrsim 4\,\mathrm{M_\odot/yr}$ for gas fractions of 10% and structural properties similar to the Milky Way. In our Galaxy, the inferred average star formation rate is only $\sim 1\,\mathrm{M_\odot/yr}$. Increasing t_*^0 by a factor of four gives therefore better agreement with the long gas consumption timescale inferred for
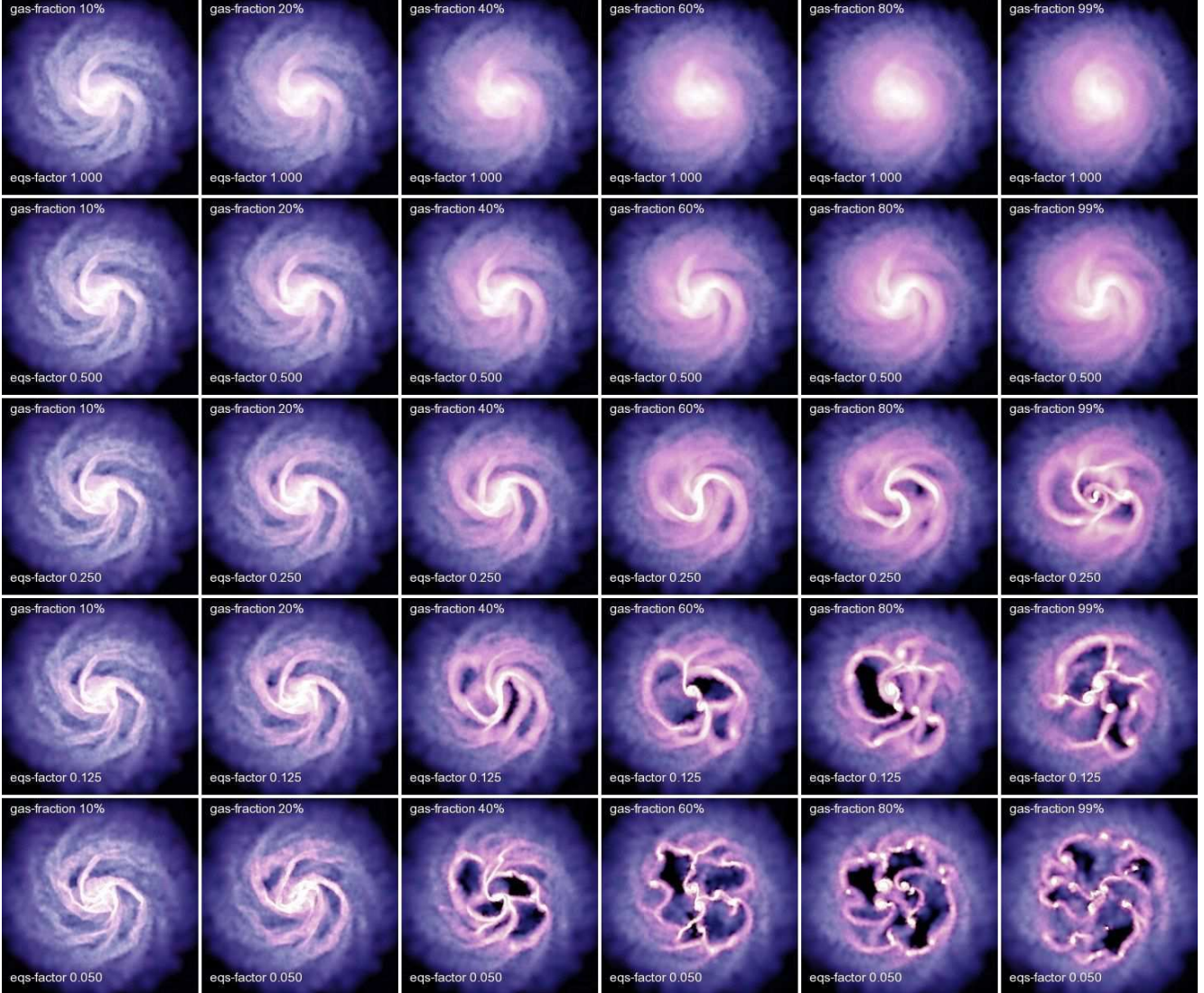
Figure 6. Stability analysis of disk galaxies as a function of gas fraction in the disk, $f_{\rm gas}$, and stiffness of the effective EOS. Each panel shows the face-on distribution of gas obtained at time $t = 0.3$ Gyrs after the start of the simulations, roughly corresponding to one rotation period at three exponential scale-lengths. The gas fraction is constant along columns, while each row shows the results for a fixed EOS. In all cases, the initial galaxy models had the same structure, except for a different partitioning of the mass in the disk between a gaseous and a stellar component. The galaxies in these examples did not include stellar bulges, but the results for galaxy models with bulges are qualitatively very similar.

the Galaxy. This also simplifies a comparison with Hernquist & Mihos (1995) and Mihos & Hernquist (1996), who chose parameters in their star formation prescription to give global star formation rates $\sim 1\,{\rm M}_\odot/{\rm yr}$ for galaxies like the Milky Way with 10% of their disk mass in gas.

Once t_*^0 is fixed, we select A_0 and $T_{\rm SN}$ as above so that the critical density for the gas to be thermally unstable, $\rho_{\rm th}$, implies a critical projected gas surface density for star formation to occur that is similar to observations (Kennicutt, 1989, 1998). Since $\rho_{\rm th}$ in our formalism depends mainly on the ratios $T_{\rm SN}/A_0$ and $T_{\rm SN}/t_*^0$, a factor of four lengthening of t_*^0 relative to SH03 requires a factor of four increase in $T_{\rm SN}$ and A_0 for a critical gas surface density $\sim 10\,{\rm M}_\odot/{\rm pc}^{-2}$ (see Figs. 2-3 of SH03). As we indicated earlier, the effective EOS depends primarily on ratios between these three parameters.

Scaling t_*^0, $T_{\rm SN}$, and A_0 by the same factor implies that the EOS for our isolated disks is the same as the "stiff" case in Figure 4, only the gas consumption timescale is larger. In the stability analysis shown below, we hold these parameters fixed, so that the threshold density for star formation is the same, but we artificially vary the stiffness of the EOS by linearly interpolating between the stiff and isothermal limits in Figure 4. EOS softenings of $q_{\rm EOS} = 1$ and $q_{\rm EOS} = 0$ refer to the stiff and isothermal cases, respectively. We also vary the fraction $f_{\rm gas}$ of the disk mass in gas, but keep the total disk mass constant.
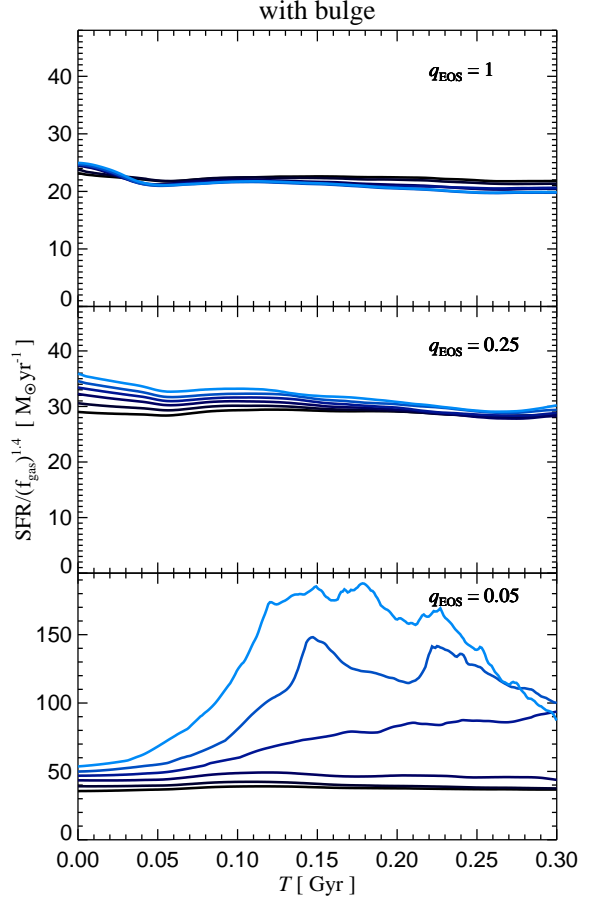
As a typical example, Figure 5 shows the time evolution of the projected gas density in an isolated galaxy model with a bulge. The gas fraction is $f_{\rm gas} = 0.1$ and the EOS softening parameter is $q_{\rm EOS} = 0.5$. Initially, the particles randomly
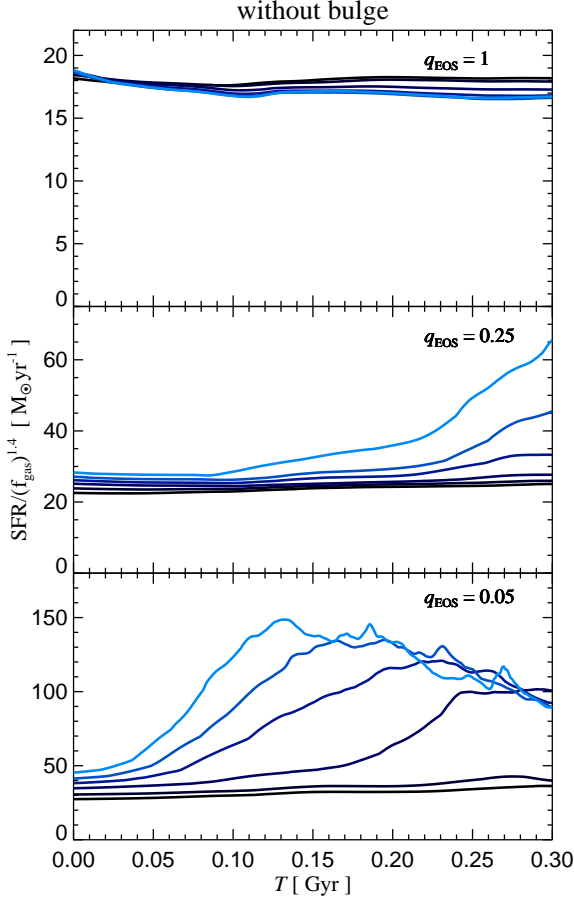
Figure 7. Evolution of the global star formation rate in galaxies without bulges, as a function of the gas fraction and EOS used. The star formation rate in solar masses per year is scaled by the disk gas fraction raised to the 1.4 power (as in the Kennicutt Law). Each panel shows the evolution for the six values of f_{gas} shown in Figure 6, with lighter colours corresponding to larger gas fractions. From top to bottom, the panels differ in the employed EOS for the star forming gas. Results are given for the stiff EOS of the multiphase model ($q_{EOS} = 1$), an intermediate case between this model and an isothermal EOS ($q_{EOS} = 0.25$), and a 'soft' model with a nearly isothermal EOS ($q_{EOS} = 0.05$).

Figure 8. Same as in Figure 7, but for galaxy models that include bulges.

sample the exponential surface density distribution, so there are no coherent structures present in the disk. However, a steady spiral pattern develops within a fraction of a rotation period owing to the action of swing amplification (Toomre, 1981). This behaviour is similar to that reported in previous numerical studies of disk structure. For the parameter choices in this example, the disk is stable for many rotation periods and does not evolve strongly. The gas is converted into stars at a relatively low rate according to our star formation prescription but, otherwise, the disk, bulge, and halo do not evolve.

However, strong, unstable evolution is possible if the gas fraction is large and the EOS is too soft. In Figure 6, we compare the distribution of gas in model galaxies without bulges after approximately one rotation period of evolution. The gas fraction is increased from $f_{gas} = 0.1$ to $f_{gas} = 0.99$

along rows (left to right) while the EOS is softened from $q_{EOS} = 1$ (top) to $q_{EOS} = 0.05$ (bottom) along columns. Some interesting features and trends are apparent from Figure 6.

First, for a relatively stiff EOS, $q_{EOS} \gtrsim 0.3$, increasing the gas fraction actually suppresses the amplitude of spiral structure in the disk. This is because in our full multiphase model, the effective temperature of the gas is $T_{eff} \gtrsim 10^5$ K over most of the disk for $q = 1$, and so the gas is dynamically hotter than the old stars. Increasing the gas fraction in this case makes the disk more stable and less susceptible to amplifying non-axisymmetric patterns. Thus, in the top row of Figure 6, the spiral structure which is apparent for $f_{gas} = 0.1$ (top left) is mostly washed out for $f_{gas} = 0.99$ (top right). This tendency does not occur if the EOS is soft because then the effective temperature is such that the gas is dynamically colder than the old stars. For $q_{EOS} \leq 0.125$ (bottom two rows), this results in unstable behaviour if the gas fraction is large.

Second, the set of models shown in Figure 6 clearly delineates stable cases from unstable ones. For our full, stiff EOS ($q_{EOS} = 1$) even pure gas disks are stable (top row). This is also true for intermediate cases with $q_{EOS} = 0.5$. However, if the effective temperature of the gas is lower than

that of the stars, very gas-rich disks are unstable and fragment within a rotation period. Thus, for example, with a nearly isothermal EOS ($q_{EOS} = 0.05$, bottom row), disks with a gas fraction $f_{gas} \gtrsim 0.3$ are already unstable (bottom row).

The previous studies by Hernquist & Mihos (1995) and Mihos & Hernquist (1996) treated the ISM as an isothermal gas and included only weak feedback in the form of a small input of random kinetic energy. These authors were unable to construct stable models with large gas fractions owing to disk fragmentation like that shown in Figure 6. Supernova feedback in our multiphase model pressurises the gas making the effective EOS stiffer, stabilising the disk.

A similar separation between stable and unstable behaviour is seen in our galaxy models that include bulges. We illustrate this in another manner in Figures 7 and 8 where we show the evolution of the global star formation rates in the disks for models without and with bulges, respectively.

The behaviour in Figures 7 and 8 clearly separates stable and unstable models. In unstable disks, fragmentation leads to a runaway growth in density perturbations, yielding unsteady evolution in the global star formation rate. Thus, all our galaxies are stable for stiff equations of state with $q_{EOS} \geq 0.5$. Models with a bulge are stable for all gas fractions with $q_{EOS} = 0.25$, however those without a bulge (Figure 7) are unstable with this EOS for $f_{gas} \gtrsim 0.6$. Softer equations of state yield unstable behaviour for galaxies without bulges for $f_{gas} \gtrsim 0.4$. For models with bulges, instability sets in at $f_{gas} > 0.8$ for $q_{EOS} = 0.125$ and $f_{gas} \gtrsim 0.6$ for $q_{EOS} = 0.05$. The scalings with q_{EOS} and f_{gas} are broadly consistent with the Toomre criterion.

6.2 Models with black holes

We have also run models similar to those described in Section 6.1, but where we added a sink particle to represent a black hole and allowed it to accrete gas from the galaxy, increasing its mass and adding a source of feedback energy in addition to supernovae. The examples we discuss in this section are not intended to provide a physical picture for the growth of supermassive black holes in isolated galaxies because we have made no attempt to tie the origin of the black holes to galaxy formation. Nevertheless, we can use these simulations to identify some generic features of our description of the interaction between black holes and the ISM that are relevant for dynamically evolving situations, like galaxy mergers.

The coupling between black hole accretion and surrounding gas has several implications. First, heating from AGN feedback energy can drive outflows from galaxies if the accretion rate is sufficiently high. This is shown in Figure 9, where the effect of black hole feedback is illustrated for an isolated galaxy with a bulge. For the low accretion rates relevant to the times indicated, the deposition of thermal energy into the gas in the vicinity of the black hole can drive a weak wind perpendicular to the plane of the disk, as indicated by the velocity vectors in this figure. These outflows are reminiscent of those in our supernova-driven winds (Figs. 5-8 in SH03). More powerful outflows can be produced during mergers when gas is driven into the centre of the remnant, fueling strong nuclear accretion.

As implied in Section 4, our description of black hole ac-
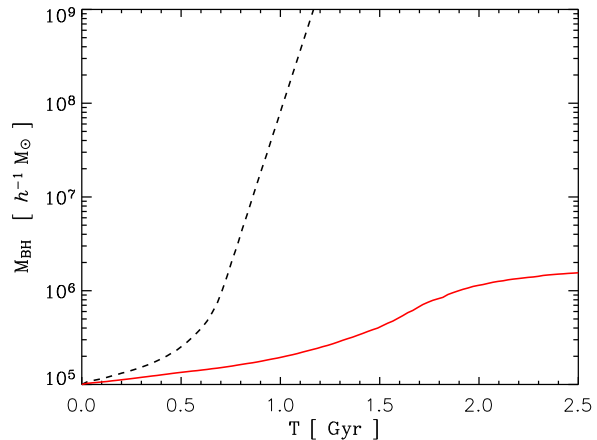
Figure 10. Evolution of the black hole mass in simulations of an isolated gas-rich galaxy. We show the black hole mass with (solid) and without (dashed) thermal feedback, respectively.

cretion yields several distinct phases of evolution, depending on the properties of the gas near the black hole. For accretion rates lower than Eddington, the black hole mass will evolve according to

$$M_{BH}(t) = \frac{M_0}{1 - \chi M_0 t}, \tag{36}$$

where M_0 is the initial black hole mass and

$$\chi = \frac{4\pi \alpha G^2 \rho}{(c_s^2 + v^2)^{3/2}}. \tag{37}$$

This result is valid only when the properties of the gas near the black hole and the relative velocity do not evolve significantly with time. When the accretion rate is higher than Eddington, the black hole grows exponentially with time,

$$M_{BH}(t) = M_{BH}(0) \exp\left(\frac{t}{t_S}\right), \tag{38}$$

where the Salpeter time,

$$t_S \equiv \frac{\epsilon_r \sigma_T c}{4\pi G m_p}, \tag{39}$$

depends only on physical constants and on the radiative efficiency. For a radiative efficiency of 10%, $t_S \approx 4.5 \times 10^7$ years.

In the absence of feedback effects, a low-mass black hole would grow first according to equation (36). Once the black hole becomes sufficiently massive, given the properties of the surrounding gas, it then enters a period of exponential growth, described by equation (38). Note that the first, Bondi-limited growth can be very slow if the initial black hole seed mass is small, or if a small value for the coefficient α is selected. We typically start our calculations with black hole seed masses of order $10^5\,M_\odot$ and set α large enough to allow a hole in a gas-rich environment to reach the Eddington regime in about $\sim 0.5\,$Gyr.

We illustrate this behaviour in Figure 10, which shows the growth of black holes in isolated, gas-rich galaxies, with and without the impact of accretion feedback on the gas. If feedback is neglected, the black hole grows in a manner
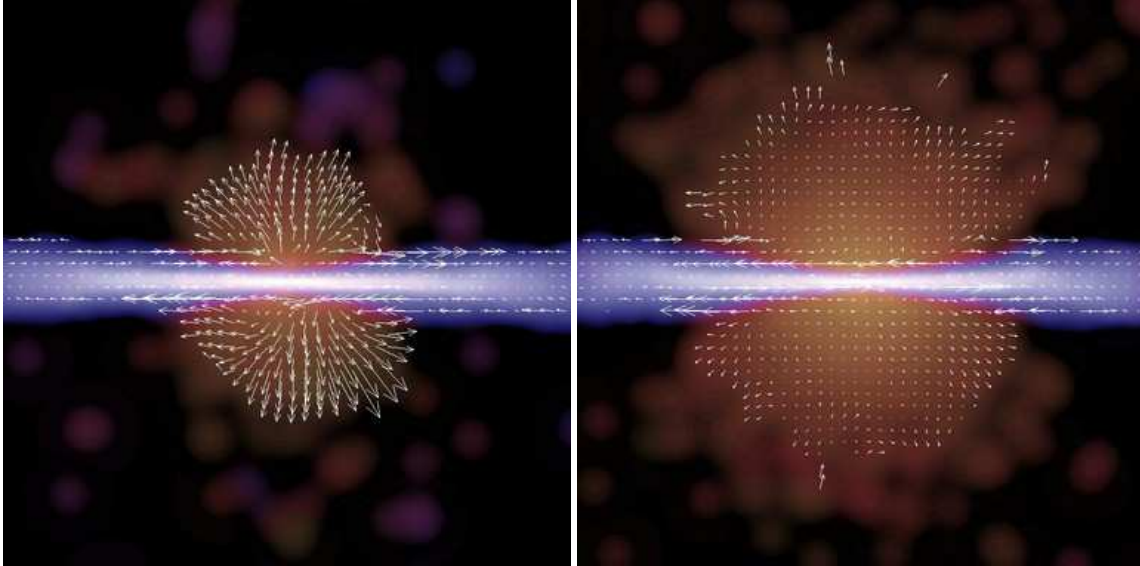
Figure 9. Edge-on view of the gas in an isolated disk galaxy with a bulge that hosts a growing, supermassive black hole in its nucleus. The two panels of side-length $32\,h^{-1}$kpc show snapshots at times 0.7 Gyrs (left) and 1.4 Gyrs (right) after the beginning of the simulation. At the low accretion rates present in this quiescent galaxy, feedback energy from the black hole can nevertheless drive a weak wind into the halo.

consistent with the expectations noted above, first according to equation (36) and later exponentially. When the effects of feedback are included, however, the growth is self-regulated and leads to a saturated final state, that depends on the initial gas content of the galaxy. The self-regulation occurs because as the accretion rate increases, the amount of energy available to affect nearby gas also grows. If this material is then heated and dispersed, the supply of gas to grow the black hole will decline as accretion is shut off.

7   MAJOR MERGERS

The approach we have adopted for handling various forms of feedback makes it possible to explore physical effects that were not accessible previously. For example, Hernquist & Mihos (1995) and Mihos & Hernquist (1996) were able to model galaxies with only small gas fractions because their treatment of feedback was insufficient to stabilise highly gas-rich disks. With our method, we can examine mergers between galaxies with a very large gas content, as might be relevant to objects at high redshifts. Also, by including processes related to black hole growth and accretion, we can study the interplay between stellar and AGN feedback that is likely to be important for understanding the nature of ultraluminous infrared galaxies (ULIRGs).

In what follows, we illustrate some of the consequences of our models for stellar and AGN feedback by looking at major mergers of disk galaxies. A representative case is given in Figure 11, which shows the distribution of gas during the merger of two equal-mass disk galaxies from a prograde, parabolic orbit. As the disks pass by one another for the first time ($t = 0.2 - 0.3$), strong tidal forces yield extended tails and bridges. Gas is shocked at the interface between the two galaxies and the tidal response drives gas into the

central regions of the two galaxies. When the galaxies finally coalesce ($t = 1.2 - 1.5$), much of the remaining gas is either converted into stars during an intense burst, or shock-heated to temperatures characteristic of the virial temperature of the remnant.

7.1   Mergers without black holes

7.1.1   Comparison with previous work

One of our goals is to see to what extent the strength of stellar feedback influences starbursts during mergers. As a starting point, we compare our results to those obtained in earlier studies, in particular, to the work of Hernquist & Mihos (1995) and Mihos & Hernquist (1996). These authors employed a highly simplified treatment of star formation by modeling the ISM as an isothermal gas with a temperature $T_{ISM} = 10^4$ K, and including a weak form of supernova feedback by injecting small amounts of kinetic energy into the gas. The amplitude of this feedback was adjusted so that isolated disks forming stars quiescently had gas profiles similar to those observed.

We have modified our simulation code to mimic the star formation and feedback algorithm of Mihos & Hernquist (1994b) in an attempt to reproduce their results. In Figure 12, we show the evolution of the star formation rate in prograde mergers of equal-mass disk galaxies with and without bulges. We have selected the parameters and galaxy models to match the results of Mihos & Hernquist (1996) as closely as possible. The results in Figure 12 can be compared directly to e.g. Fig. 5a in Mihos & Hernquist (1996).

The morphologies of the merging galaxies roughly follows the time sequence in Figure 11, with only a modest dependence on their structural properties. When the galaxies first pass by one another, relatively strong star-
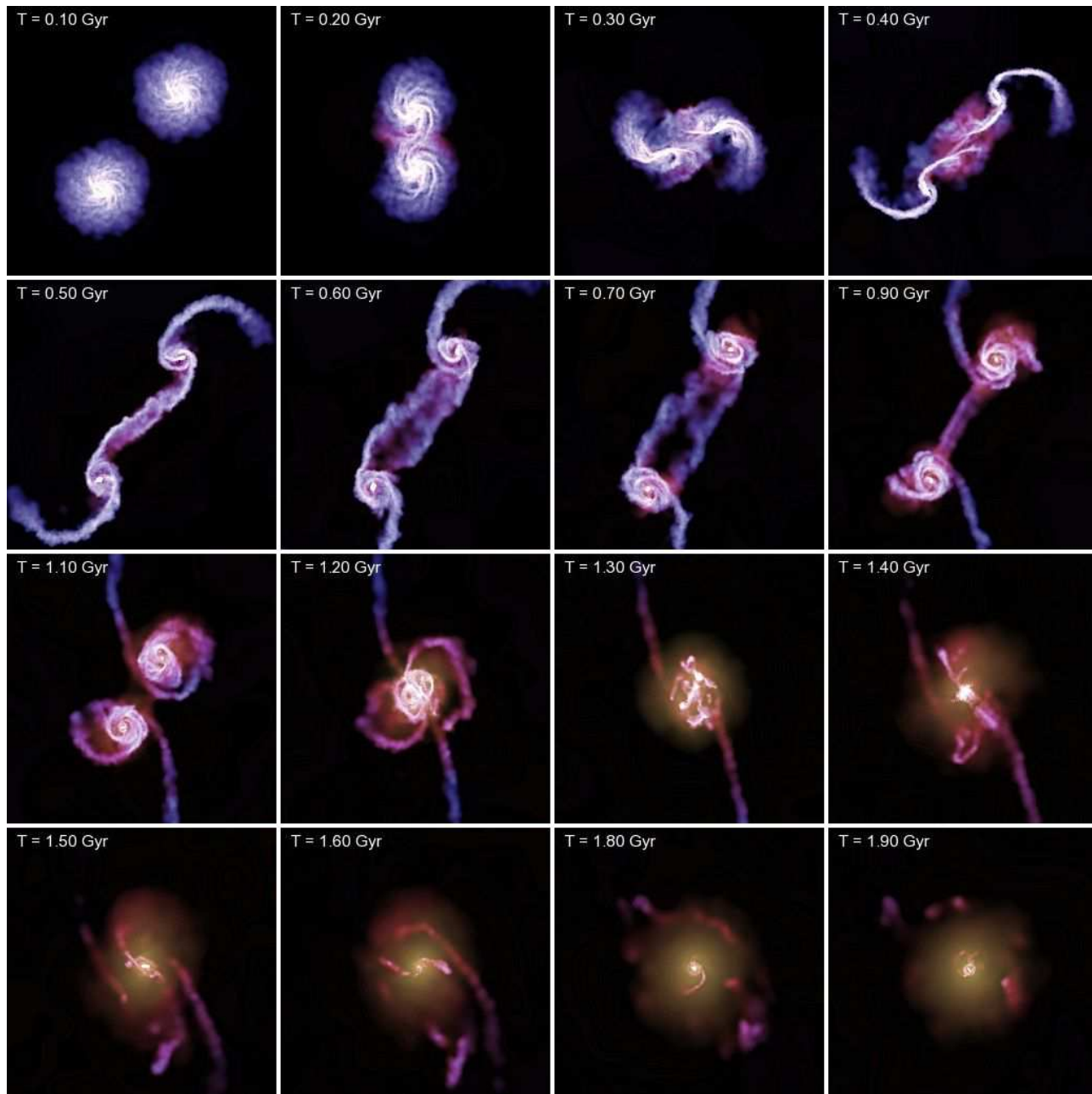
Figure 11. Evolution of the gas distribution in a major merger of two disk galaxies. Colour hue encodes gas temperature, while brightness indicates gas density. Each frame measures $50 \, h^{-1}$kpc on a side, and the corresponding time of each image is given by the labels. In this simulation, a slightly softer EOS ($q_{\rm EOS} = 0.25$) than in our default multiphase model was used.

bursts are triggered in each disk in the case when bulges are not present. Galaxies with bulges experience much weaker starbursts during first passage. Mihos & Hernquist (1996) showed that this difference arises from the relative ease with which the disks can amplify $m = 2$ disturbances in response to tidal forcing. During final coalescence, a much strong starburst is excited in the models with bulges because much of the gas in the bulgeless galaxies has already been consumed by this time. These trends agree well with those identified by Mihos & Hernquist (1996).

The amplitudes of the starbursts shown in Figure 12 are

comparable to, but somewhat stronger than those shown in Fig. 5a of Mihos & Hernquist (1996), and considerably stronger than those found by Barnes (2004) (see e.g. his Fig. 5). By varying the parameters of our simulations, we have found that the evolution of the star formation rate in mergers with only relatively weak feedback is sensitive to numerical resolution. If the star formation rate is tied to gas density, the amplitudes of merger-induced starbursts depend on the compressibility of the gas, which is influenced by both the stiffness of the EOS, as well as dynamic range in resolution of the numerical algorithm. We have verified that
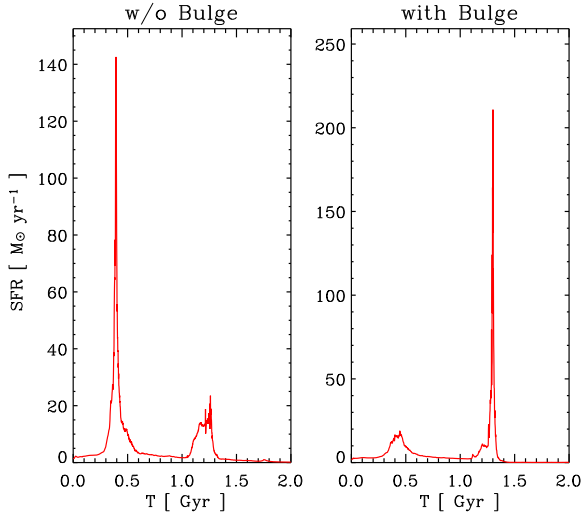
Figure 12. Evolution of the star formation rate in major mergers of disk galaxies, using a description of the ISM that mimics the approach of Hernquist & Mihos (1995) and Mihos & Hernquist (1996). We show results for models without (left) and with (right) bulges. The galaxies have the rotation curves shown in Figure 3, and the disks initially consisted of 10% gas.
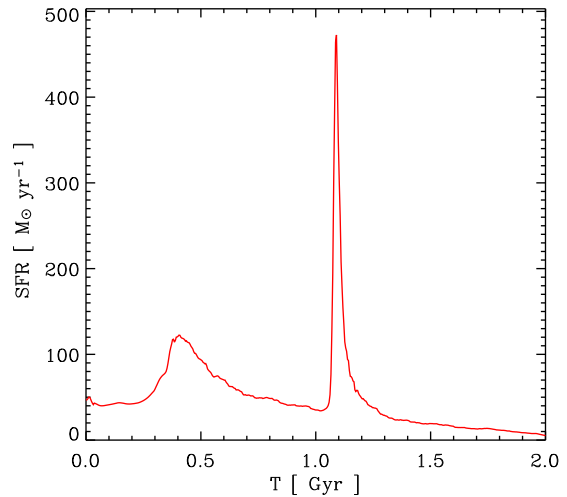

Figure 13. Evolution of the star formation rate in a major merger of two disk galaxies without bulges, and with disks that initially consisted of 99.9% gas.

differences in resolution are mainly responsible for the residual discrepancies between the star formation rates shown in Figure 12 and those reported by Mihos & Hernquist (1996) and Barnes (2004).

7.1.2   Multiphase treatment of ISM

As a next step, we have performed a grid of merger simulations using the multiphase treatment of supernova feedback described in Section 3. We have varied the structural properties of the galaxies, the orbit of the mergers, and the parameters in our multiphase model. Below, we limit the discussion mainly to the consequences of variations in the fraction of gas in each galaxy and the strength of feedback to highlight the new types of outcomes that are possible.

In Figure 13, we show the evolution of the star formation rate from one of our simulations, a prograde, major merger of two disk galaxies without bulges. In this case, each disk initially consisted of $f_{gas} = 99.9\%$ gas and only 0.1% of old stars. The EOS was relatively stiff with a softening parameter of $q_{EOS} = 0.5$. (That is, the EOS was linearly interpolated to lie midway between the curves in Figure 4 for $\rho > \rho_{th}$.) Even with this extreme gas content, the model disks are stable in isolation, owing to the pressurisation of the gas from supernova feedback. The parameters of this simulation are deliberately chosen to be extreme to simplify the discussion, but qualitatively similar results are obtained in more general situations.

In the example shown in Figure 13 the star formation rate peaks at roughly $500\,\mathrm{M_\odot yr^{-1}}$, considerably higher than in earlier simulations of equal-mass mergers of disks, owing to the large gas content of each galaxy. Star formation rates at this level are similar to those inferred for systems at high redshift such as Lyman-break galaxies and SCUBA sources,

suggesting that some of these objects may result from mergers of gas-rich disks.

Figure 13 also demonstrates that while the general conclusions of Mihos & Hernquist (1996) are obtained under broader circumstances, some of their results clearly depend on the strength of feedback from star formation. In models with weak supernova feedback, as in Figure 12, galaxies without bulges experience stronger starbursts at first passage than during final coalescence. The evolution shown in Figure 13 is rather different, with the strongest starburst accompanying the final merger. While the merging galaxies in this example still develop a bar-like structure in response to tidal forcing, the gas is sufficiently hot dynamically that it is not strongly compressed during this phase of evolution, limiting the strength of the initial starburst. The more intense starburst during the final merger results from strong shock compression of the gas and gravitational torquing when the galaxies coalesce, in a manner reminiscent of the mergers with bulges examined by Mihos & Hernquist (1996); Barnes & Hernquist (1991, 1996).

An interesting aspect of the simulation used in Figure 13 concerns the structure of the merger remnant. A considerable amount of gas is left behind following the merger. Much of it settles into an extended disk, surrounding a relatively compact, rapidly rotating remnant of newly formed stars. Overall, the remnant is morphologically closer to a spiral galaxy with a bulge than to an elliptical. Further implications and a detailed analysis of this simulation are presented in Springel & Hernquist (2004).

7.2   Mergers with black holes

An even greater diversity of outcomes results during a merger if the impact of central, supermassive black holes is included in addition to feedback from star formation. As we discuss in Di Matteo et al. (2004b) and Springel et al. (2004), mergers of galaxies that involve star formation, supernova

feedback, black hole growth and accretion, and AGN feedback yield a generic time history in which the tidal interaction drives gas into the centre of the remnant, fueling a starburst and triggering the rapid growth of the central black hole(s). Feedback from accretion onto the black hole(s) influences the thermodynamic properties of the surrounding gas, eventually expelling it from the inner regions of the remnant, terminating the episode of rapid star formation and self-limiting the growth of the black hole(s). The starburst and AGN activity are coeval, but offset in time owing to the detailed form of the response of the gas to the feedback. Thus, while we expect starbursts and AGN activity to be correlated in this picture, the remnant will be primarily seen in different stages as the merger progresses and will evolve from one type of object into the other, depending on the observed wavelength regime.

In Figure 14 we show three snapshots from a simulation that includes our model for the growth of black holes. In this example, the galaxies included bulges and the disks were 10% gas. Following the first passage (shown on the left), but before the galaxies coalesce, the disks are distorted by their mutual tidal interaction, but only a relatively weak starburst is triggered, because the bulges stabilise the disks against a strong $m = 2$ response. The black holes do not accrete significantly during this phase of evolution, and so neither galaxy would be observable as an AGN. When the galaxies merge but before the gas has been consumed (middle), tidal forces trigger a nuclear starburst and fuel rapid growth of the black holes. The peak in the starburst occurs near the time indicated in Figure 14, but the peak in the black hole growth is offset, owing to the delayed action of AGN feedback on the gas. In principle, the system should now be both a starburst and an AGN, but it is likely that the quasar-activity would be obscured by surrounding gas and dust, at least during the beginning of the burst. Only during the final stages of evolution could the remnant be visible as an AGN, when outflows remove the dense layers of gas around it.

As the remnant settles into a relaxed state, star formation and black hole accretion are rapidly quenched by the expulsion of gas from the centre, as a consequence of AGN feedback. The remnant would no longer be observable as either a starburst or an AGN and will age rapidly, quickly resembling an evolved red galaxy (Springel et al., 2004). At this point the black hole growth ceases and the black hole mass attained is consistent with those expected from the observed $M_{\rm BH} - \sigma$ relation (Di Matteo et al., 2004b).

The interplay between black hole growth and the physics of the ISM in simulations like that shown in Figure 14 has significant implications for the observed properties of these systems. In Figure 15, we show the evolution of the intrinsic star formation rates in simulations of galaxy mergers with and without bulges and including or neglecting central black holes. This figure shows that the presence of the black holes and the feedback energy derived from their growth can dramatically alter the nature of the starburst resulting from a merger. The peak amplitude of the starburst in the merger which included bulges is lowered by about a factor of five, owing to AGN feedback. We note, however, that the observed emission from such an object would include both the radiation from the starburst as well as the energy output from black hole accretion. If most of the AGN emission is reprocessed into optical or infrared ra-
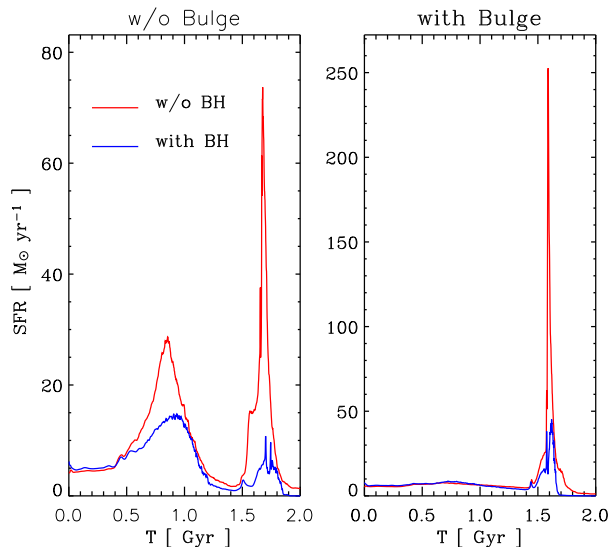

Figure 15. Star formation rates in mergers of galaxies without (left) and with (right) bulges. In each panel, the two curves show the outcome with and without black holes.

diation by surrounding gas and dust before it escapes from the inner regions of the remnant, it could be incorrectly attributed to the starburst, rather than being associated with a buried quasar. A more complete understanding of the implications of these results will require a detailed modeling of the spectral energy distribution from the combination of the starburst and the obscured AGN.

We have varied the orbital geometry and structural properties of the merging galaxies to see if the results described above are generic. While the detailed outcome does depend on e.g. the orbit, many of the overall properties are relatively unaffected. An example is shown in Figure 16 where the evolution of the total black hole mass is given for six different orbital configurations. The top three panels show prograde-prograde, prograde-retrograde, and retrograde-retrograde mergers (left to right), while the bottom three panels show cases where the disk orientations were chosen randomly. While the detailed response varies from model to model, the final total black hole mass is insensitive to the orbital parameters. In all cases, the final black hole mass is $\sim 2 - 3 \times 10^7 \, {\rm M_\odot}$. This value is consistent with the observed correlation between black hole and spheroid mass for the remnants produced in these mergers, as shown in more detail in Di Matteo et al. (2004b). The simulation results are in accord with the view that black hole growth is regulated by AGN feedback and the dynamical response of gas to this supply of energy.

We note that in our model the AGN feedback energy is deposited isotropically in the gas around the black hole. While this appears to be a natural approximation given that we cannot resolve the detailed accretion physics close to the hole, observations show that black hole outflows are typically bi-polar (although not necessarily strongly collimated) and often result from powerful jets. It is possible that our isotropic coupling enhances the effects of the feedback, but this effect should be compensated in part by our comparatively conservative assumption for $\epsilon_{\rm f}$. We also caution that the physical nature of the coupling of AGN feedback to the
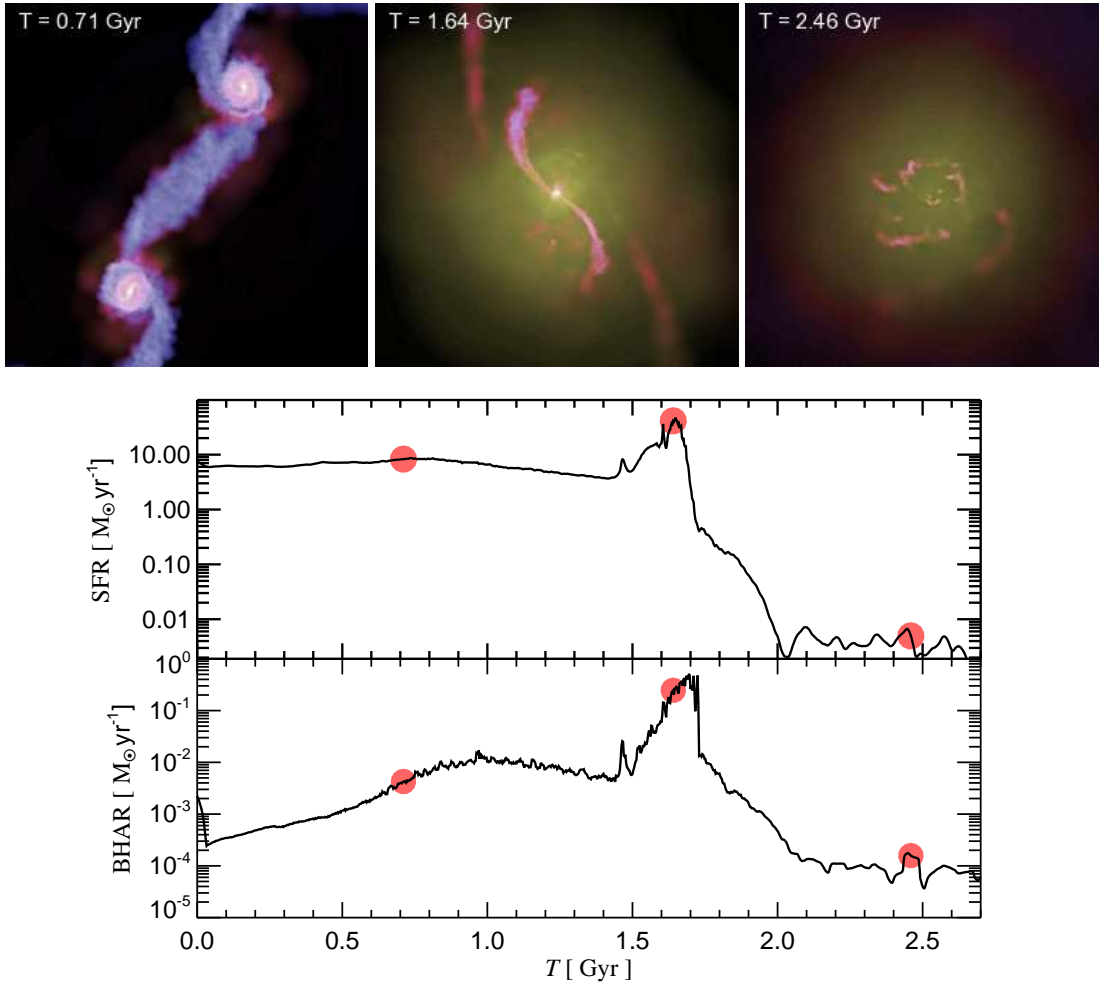
Figure 14. Merger of two disk galaxies, including the effects of black hole growth and AGN feedback. The images show the gas distribution in the two disks at three different times, where colour hue encodes temperature while brightness measures gas density. The bottom panels show the time evolution of the accretion rate onto the black holes (top) and the star formation rate (bottom). The red symbols in these panels mark the three times shown in the images on top. The first snapshot shows the system just after the first passage of the two disks. The second snapshot captures the system when the galaxies are coalescing, at which point the star formation and accretion rates peak. Finally, the third snapshot shows the system after the galaxies have fully merged, and most of the mass has settled into a slowly evolving remnant.

surrounding gas is not fully understood yet. In particular, there may be important feedback mechanisms other than thermal heating. For example, radiation pressure may play a very important role as well (Murray et al., 2004).

The presence of central black holes can also have a significant impact on the stellar density structure of merger remnants. Mihos & Hernquist (1994a) found that their remnants typically had centrally peaked luminosity profiles from the compact stellar cores left behind by starbursts. In our new simulations, the remnants have smoother luminosity profiles into their centres, in much better agreement with observations of elliptical galaxies (Springel, Di Matteo & Hernquist, 2004, in preparation). This outcome is driven by a combination of the consumption of dense gas by the black holes, the dynamical heating of the gas as the black holes spiral together and merge, and the dispersal of gas by AGN feedback. Our results thus indicate that black hole growth may be an integral part of spheroid formation.

8 CONCLUSIONS

In this paper, we have introduced a new methodology for simultaneously modeling star formation and black hole accretion in hydrodynamical simulations of isolated and merging galaxies. Our approach uses the concept of forming "macroscopic", coarse-grained representations of sub-resolution physics, allowing us to study the effects of these processes on larger, resolved scales. To illustrate the principal effects of our methods and of the physics we describe, we have focused on simulations of isolated and merging galaxies. Throughout, we have concentrated on the methodological aspects of our work, rather than on an in-depth analysis of the physical results of our simulations. We provide the latter in related papers (e.g. Di Matteo et al., 2004b; Springel et al., 2004).

For our simulations, we have constructed compound galaxy models that consist of a dark matter halo, a rotationally supported disk of gas and stars, and a central bulge,
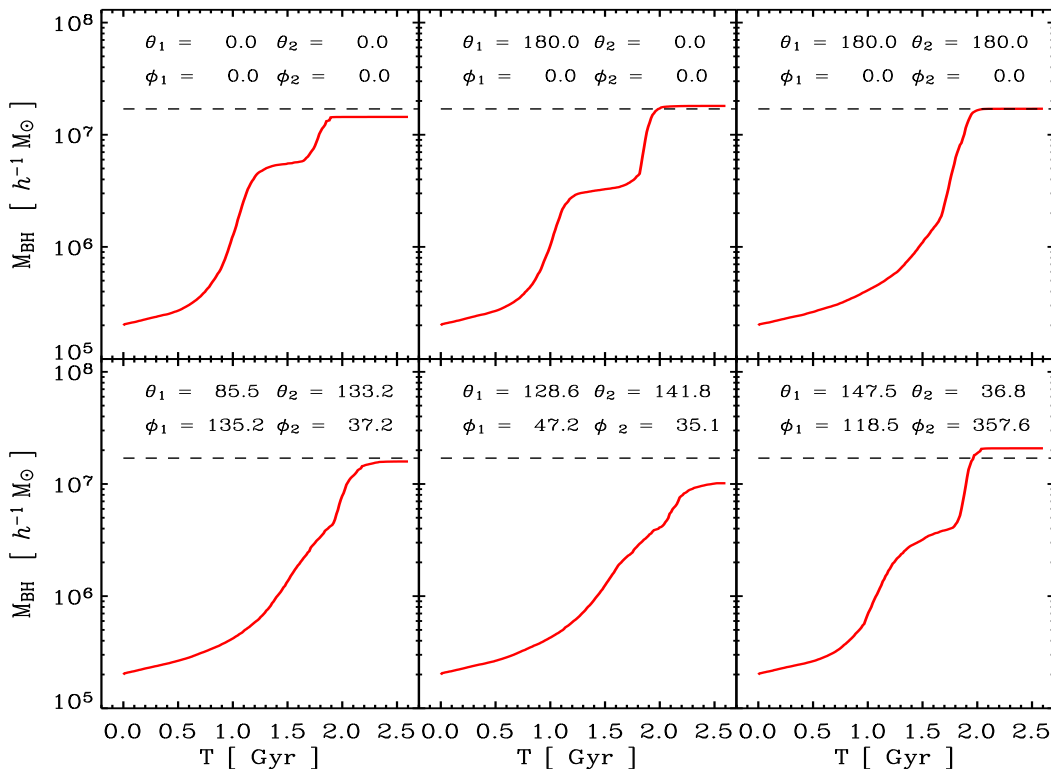
Figure 16. Evolution of the total black hole mass in merger simulations that differ in their encounter geometries. The top three panels show results where the disks are oriented in the orbital plane, while the bottom three panels are for simulations with random disk orientations. The angles (θ, ϕ) specify the orientation of the spin vector of one of the disk galaxies relative to the orbital plane (see Duc et al., 2000, for a sketch of the orbital configuration).

with independent parameters describing each of the structural components. Our approach improves upon previous methods by accounting for gas pressure forces, as well as featuring a flexible numerical approach for computing the gravitational potential for non-trivial, radially varying mass distributions in the disk. As a result, we are able to construct very stable disk galaxy models even for high gas fractions.

In simulations of isolated galaxies, we have emphasised the importance of the treatment of feedback processes in the dense star-forming ISM for the stability of disk galaxies. Simulations that use a simple isothermal equation of state, or a weak form of kinetic feedback, have gas disks that are very susceptible to axisymmetric perturbations. As a result, galaxies with large gas surface mass density cannot be evolved in a stable fashion for a long time in such models. Our multiphase model for the ISM encapsulates the effects of local supernova feedback in the form of an EOS, which is comparatively stiff. When this description for the ISM is chosen, the dense gas is stabilised by supernovae pressurising the gas, so that much larger gas fractions than in previous studies become possible.

We used simulations of isolated galaxy models to examine the properties of the various phases of accretion possible in our model for the growth of black holes. In particular, we showed how the black hole growth of a small seed black hole accelerates in the Bondi regime and eventually reaches Eddington-limited, exponential growth. However, the growth process can be slowed down and regulated

by the feedback energy associated with the accretion. We assumed a simple thermal coupling of a small fraction of the hole's bolometric luminosity to the surrounding gas; this can increase the local sound speed of the gas and thereby reduce the Bondi accretion rate, or in extreme cases of high accretion, generate a powerful, pressure-driven quasar wind.

Using a number of simulations of major galaxy mergers, both with and without black holes, we have explored a few basic consequences of our methods. When we model the star-forming gas with an isothermal equation of state and weak feedback, our results are in good agreement with previous work by Mihos & Hernquist (1996). However, our multiphase treatment of the ISM allows us to investigate galaxy mergers with much higher gas fractions than possible before. Here, new types of outcomes are possible for major mergers. For example, very high star formation rates of several hundred solar masses per year can be reached in gas-rich mergers. In merger simulations with black holes we have shown that the presence of accreting black holes can dramatically alter the dynamics of the merger. The feedback energy associated with the growth of the hole owing to the tidally triggered inflow of gas has a direct effect on the strength of the nuclear starburst. During the final galaxy coalescence, the BH can expel the gas from the centre in a powerful outflow, quenching the starburst on a short timescale. The resulting elliptical remnant is then gas-poor and reddens quickly.

Already, these exploratory results show clearly that adding an accreting supermassive black hole in the cen-

tre can have a decisive influence on galaxies. In fact, we think this indicates that the build-up of supermassive black holes and massive galaxies are an intertwined process which requires a self-consistent treatment to be meaningfully addressed. Our new numerical methodology represents the first attempt to do carry out this demanding task in cosmological hydrodynamical simulations, opening up the possibility to jointly study the formation of galaxies and the build-up of supermassive black holes hosted by them. Our methods thus provide a powerful tool to gain new insights into the process of hierarchical galaxy formation.

REFERENCES

Barnes J., Hut P., 1986, Nature, 324, 446
Barnes J. E., 1988, ApJ, 331, 699
Barnes J. E., 1992, ApJ, 393, 484
Barnes J. E., 2004, MNRAS, 350, 798
Barnes J. E., Hernquist L., 1992, ARA&A, 30, 705
Barnes J. E., Hernquist L., 1996, ApJ, 471, 115
Barnes J. E., Hernquist L. E., 1991, ApJL, 370, L65
Binney J., Tremaine S., 1987, Galactic Dynamics, Princeton Univ. Press, Princeton
Bondi H., 1952, MNRAS, 112, 195
Bondi H., Hoyle F., 1944, MNRAS, 104, 273
Chartas G., Brandt W. N., Gallagher S. C., 2003, ApJ, 595, 85
Crenshaw D. M., Kraemer S. B., George I. M., 2003, ARA&A, 41, 117
Di Matteo T., Croft R. A. C., Springel V., Hernquist L., 2003, ApJ, 593, 56
Di Matteo T., Croft R. A. C., Springel V., Hernquist L., 2004a, ApJ, 610, 80
Di Matteo T., Springel V., Hernquist L., 2004b, submitted
Dubinski J., Carlberg R. G., 1991, ApJ, 378, 496
Dubinski J., Mihos J. C., Hernquist L., 1996, ApJ, 462, 576
Dubinski J., Mihos J. C., Hernquist L., 1999, ApJ, 526, 607
Duc P.-A., Brinks E., Springel V., Pichardo B., Weilbacher P., Mirabel I. F., 2000, AJ, 120, 1238
Escala A., Larson R. B., Coppi P. S., Mardones D., 2004, ApJ, 607, 765
Fabian A. C., 1999, MNRAS, 308, L39
Ferrarese L., Merritt D., 2000, ApJL, 539, L9
Gebhardt K., Bender R., Bower G., et al., 2000, ApJL, 539, L13
Gerritsen J. P. E., Icke V., 1997, A&A, 325, 972
Gingold R. A., Monaghan J. J., 1977, MNRAS, 181, 375
Granato G. L., De Zotti G., Silva L., Bressan A., Danese L., 2004, ApJ, 600, 580
Haiman Z., Ciotti L., Ostriker J. P., 2004, ApJ, 606, 763
Hernquist L., 1989, Nature, 340, 687
Hernquist L., 1990, ApJ, 356, 359
Hernquist L., 1992, ApJ, 400, 460
Hernquist L., 1993a, ApJS, 86, 389
Hernquist L., 1993b, ApJ, 404, 717
Hernquist L., 1993c, ApJ, 409, 548
Hernquist L., Katz N., 1989, ApJS, 70, 419
Hernquist L., Mihos J. C., 1995, ApJ, 448, 41
Hernquist L., Springel V., 2003, MNRAS, 341, 1253
Hoyle F., Lyttleton R. A., 1939, in Proceedings of the Cambridge Philisophical Society, 405
Jogee S., 2004, in AGN Physics on All Scales
Katz N., Weinberg D. H., Hernquist L., 1996, ApJS, 105, 19
Kauffmann G., Haehnelt M., 2000, MNRAS, 311, 576
Kazantzidis S., Magorrian J., Moore B., 2004, ApJ, 601, 37
Kennicutt R. C., 1989, ApJ, 344, 685
Kennicutt R. C., 1998, ApJ, 498, 541
King A., 2003, ApJL, 596, L27
Kormendy J., Gebhardt K., 2001, in AIP Conf. Proc. 586: 20th Texas Symposium on relativistic astrophysics, 363
Kormendy J., Richstone D., 1995, ARA&A, 33, 581
Lucy L. B., 1977, AJ, 82, 1013
Magorrian J., Tremaine S., Richstone D., et al., 1998, AJ, 115, 2285
Makino J., Funato Y., 2004, ApJ, 602, 93
Marconi A., Hunt L. K., 2003, ApJL, 589, L21
McLure R. J., Dunlop J. S., 2002, MNRAS, 331, 795
Melnick J., Mirabel I. F., 1990, A&A, 231, L19
Mihos J. C., Dubinski J., Hernquist L., 1998, ApJ, 494, 183
Mihos J. C., Hernquist L., 1994a, ApJL, 437, L47
Mihos J. C., Hernquist L., 1994b, ApJ, 437, 611
Mihos J. C., Hernquist L., 1996, ApJ, 464, 641
Mo H. J., Mao S., White S. D. M., 1998, MNRAS, 295, 319
Monaghan J. J., 1992, ARA&A, 30, 543
Murray N., Quataert E., Thompson T. A., 2004, astro-ph/0406070
Navarro J. F., Frenk C. S., White S. D. M., 1996, ApJ, 462, 563
Negroponte J., White S. D. M., 1983, MNRAS, 205, 1009
Pounds K. A., Reeves J. N., King A. R., Page K. L., O'Brien P. T., Turner M. J. L., 2003, MNRAS, 345, 705
Rawlings S., Saunders R., 1991, Nature, 349, 138
Rines K., Geller M. J., Diaferio A., Kurtz M. J., Jarrett T. H., 2004, AJ, 128, 1078
Rines K., Geller M. J., Diaferio A., Mahdavi A., Mohr J. J., Wegner G., 2002, AJ, 124, 1266
Rines K., Geller M. J., Diaferio A., Mohr J. J., Wegner G. A., 2000, AJ, 120, 2338
Rines K., Geller M. J., Kurtz M. J., Diaferio A., 2003, AJ, 126, 2152
Robertson B., Yoshida N., Springel V., Hernquist L., 2004, ApJ, 606, 32
Sanders D. B., Soifer B. T., Elias J. H., et al., 1988, ApJ, 325, 74
Shakura N. I., Sunyaev R. A., 1973, A&A, 24, 337
Silk J., Rees M. J., 1998, A&A, 331, L1
Springel V., 2000, MNRAS, 312, 859
Springel V., Di Matteo T., Hernquist L., 2004, astro-ph/0409436
Springel V., Hernquist L., 2002, MNRAS, 333, 649
Springel V., Hernquist L., 2003a, MNRAS, 339, 289
Springel V., Hernquist L., 2003b, MNRAS, 339, 312
Springel V., Hernquist L., 2004, in preparation
Springel V., White S. D. M., 1999, MNRAS, 307, 162
Springel V., Yoshida N., White S. D. M., 2001, New Astronomy, 6, 79
Tavecchio F., Maraschi L., Ghisellini G., et al., 2000, ApJ, 543, 535
Toomre A., 1964, ApJ, 139, 1217
Toomre A., 1977, in Evolution of Galaxies and Stellar Populations, 401, Yale Univ. Obs: New Haven
Toomre A., 1981, in Structure and Evolution of Normal Galaxies, 111–136, Cambridge Univ. Press: Cambridge
Toomre A., Toomre J., 1972, ApJ, 178, 623
Tremaine S., Gebhardt K., Bender R., et al., 2002, ApJ, 574, 740
Volonteri M., Haardt F., Madau P., 2003, ApJ, 582, 559
Wyithe J. S. B., Loeb A., 2003, ApJ, 595, 614